Article

Neuron

Mossy Cells Control Adult Neural Stem Cell Quiescence and Maintenance through a Dynamic Balance between Direct and Indirect Pathways

Graphical Abstract

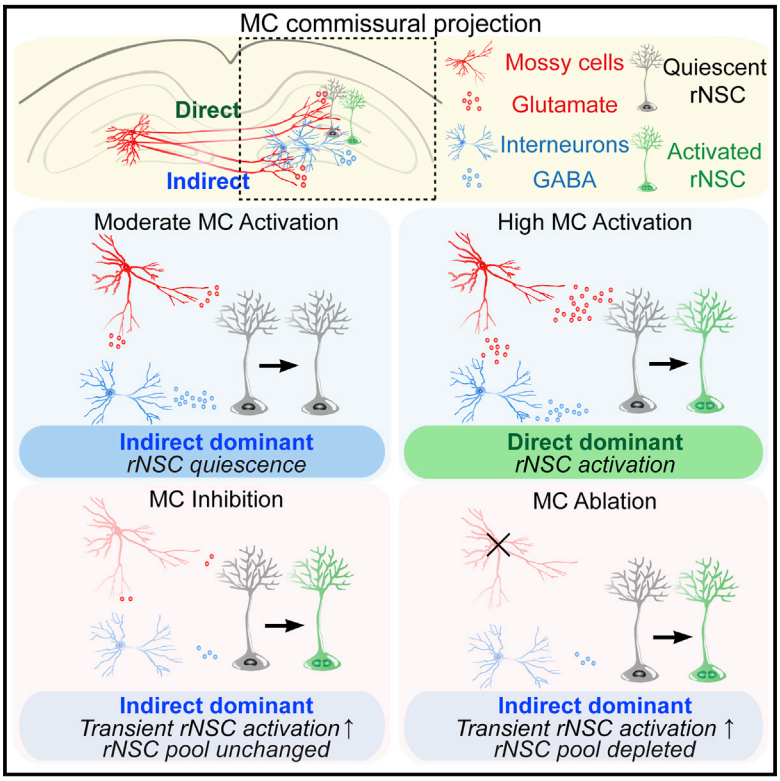

Highlights

- MCs regulate NSCs through a balance between direct and indirect pathways
- NSC quiescence is differentially regulated by distinct MC activity states
- A small population of MCs exert a significant impact on NSC quiescence
- MC loss leads to transient activation of NSCs followed by pool depletion

Authors

Chia-Yu Yeh, Brent Asrican, Jonathan Moss, ..., Wei Lu, Nicolas Toni, Juan Song

Correspondence

juansong@email.unc.edu

In Brief

Yeh et al. demonstrate that mossy cells regulate adult NSCs through direct glutamatergic and indirect GABAergic pathways. Functionally, mossy cells at various activity states control NSC quiescence and maintenance through a dynamic balance of glutamatergic and GABAergic signaling onto NSCs.

Yeh et al., 2018, Neuron *99*, 493–510
August 8, 2018
https://doi.org/10.1016/j.neuron.2018.07.010

CellPress

Neuron
Article

Mossy Cells Control Adult Neural Stem Cell Quiescence and Maintenance through a Dynamic Balance between Direct and Indirect Pathways

Chia-Yu Yeh,[1,7] Brent Asrican,[1,7] Jonathan Moss,[5,8] Luis Jhoan Quintanilla,[1,3,8] Ting He,[1] Xia Mao,[4] Frederic Cassé,[5,6] Elias Gebara,[5] Hechen Bao,[1] Wei Lu,[4] Nicolas Toni,[5,6,9] and Juan Song[1,2,9,10,*]
[1]Department of Pharmacology, University of North Carolina, Chapel Hill, NC 27599, USA
[2]Neuroscience Center, University of North Carolina, Chapel Hill, NC 27599, USA
[3]Neuroscience Curriculum, University of North Carolina, Chapel Hill, NC 27599, USA
[4]Synapse and Neural Circuit Research Unit, National Institute of Neurological Disorders and Stroke, National Institutes of Health, Bethesda, MD 20892, USA
[5]Department of Fundamental Neurosciences, University of Lausanne, 1005 Lausanne, Switzerland
[6]Centre for Psychiatric Neuroscience, Department of Psychiatry, Lausanne University Hospital, 1008 Prilly-Lausanne, Switzerland
[7]These authors contributed equally
[8]These authors contributed equally
[9]These authors contributed equally
[10]Lead Contact
*Correspondence: juansong@email.unc.edu
https://doi.org/10.1016/j.neuron.2018.07.010

SUMMARY

Mossy cells (MCs) represent a major population of excitatory neurons in the adult dentate gyrus, a brain region where new neurons are generated from radial neural stem cells (rNSCs) throughout life. Little is known about the role of MCs in regulating rNSCs. Here we demonstrate that MC commissural projections structurally and functionally interact with rNSCs through both the direct glutamatergic MC-rNSC pathway and the indirect GABAergic MC-local interneuron-rNSC pathway. Specifically, moderate MC activation increases rNSC quiescence through the dominant indirect pathway, while high MC activation increases rNSC activation through the dominant direct pathway. In contrast, MC inhibition or ablation leads to a transient increase of rNSC activation, but rNSC depletion only occurs after chronic ablation of MCs. Together, our study identifies MCs as a critical stem cell niche component that dynamically controls adult NSC quiescence and maintenance under various MC activity states through a balance of direct glutamatergic and indirect GABAergic signaling onto rNSCs.

INTRODUCTION

Adult hippocampal neurogenesis arises from radial neural stem cells (rNSCs) within a specialized local niche in the adult dentate gyrus (DG). Neuronal activity and experience, acting on this local niche, regulate rNSCs and subsequent hippocampal neurogenesis (Song et al., 2012, 2016). Within the DG neurogenic niche, mossy cells (MCs) are one of the major glutamatergic neurons and innervate both mature granule cells (GCs) and local interneurons that make GABAergic synapses onto GCs (Scharfman, 1995). Recently, MCs have received tremendous attention because of their critical roles in cognition, their vulnerability to glutamate excitotoxicity in temporal lobe epilepsy, and their potential involvement in neuropsychiatric disorders (Scharfman, 2016). To date, very few studies have examined the influence of MCs on hippocampal neurogenesis, though it has been suggested that MCs could be important because they provide the first glutamatergic synaptic inputs, as well as disynaptic GABAergic inputs, onto newborn GCs (Chancey et al., 2014; Deshpande et al., 2013; Vivar et al., 2012). MCs project axons along the septo-temporal axis of the ipsilateral DG (associational pathway) as well as to the contralateral DG (commissural pathway) (Buckmaster et al., 1996). These axons target the inner molecular layer (IML) of the DG and extend collaterals within the hilus (Scharfman and Myers, 2013). The localization of MC collaterals in the IML and hilus is particularly intriguing because it is closely associated with the neurogenic niche where rNSCs and local interneurons reside. It remains unknown whether and how MCs contribute to the functional regulation of rNSCs and subsequent hippocampal neurogenesis.

Using an array of circuit-based approaches in combination with stereological analysis of rNSCs, we demonstrate that MC commissural projections structurally and functionally interact with rNSCs through both the direct glutamatergic MC-rNSC pathway and the indirect GABAergic MC-local interneuron-rNSC pathway. Strikingly, rNSC quiescence is dynamically regulated through the balance of direct and indirect pathways onto rNSCs under various MC activity states. Under a moderate MC activation state, MCs increase rNSC quiescence through the dominant indirect pathway. In contrast, under a high MC activation state, MCs increase rNSC activation through the dominant direct pathway. Interestingly, both inhibition and chronic ablation

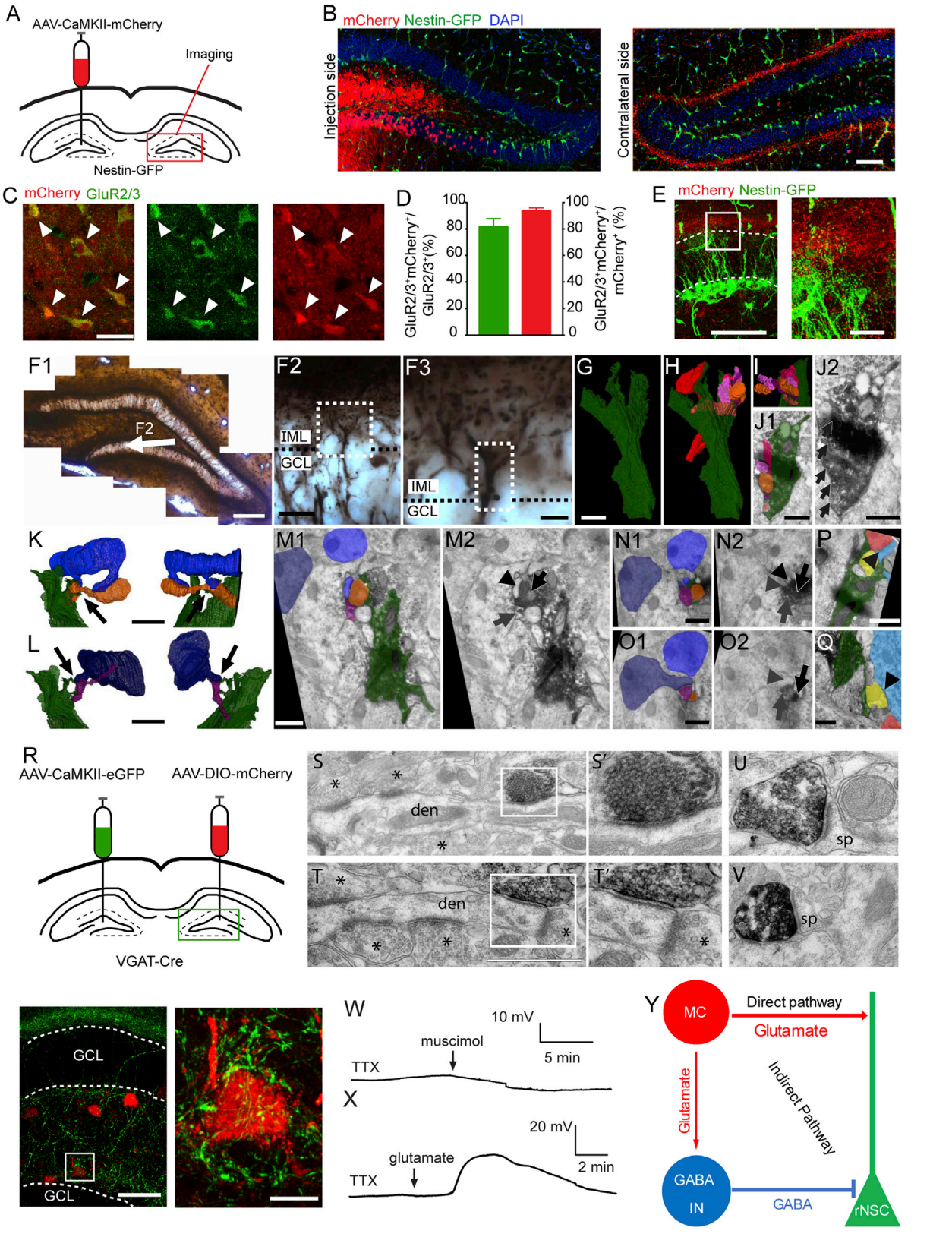

(legend on next page)

of MCs lead to a transient increase of rNSC activation, likely due to reduced GABA signaling mediated by the indirect pathway, but rNSC depletion only occurs upon chronic ablation of MCs. These results suggest that MC inhibition and ablation represent distinct MC activity patterns onto rNSCs. In summary, our study identifies MCs as a critical stem cell niche component that controls rNSC quiescence and long-term maintenance under various MC activity states through a dynamic balance of direct and indirect pathways onto rNSCs.

RESULTS

MC Commissural Projections Structurally Interact with rNSCs through Both Direct Glutamatergic and Indirect GABAergic Pathways

To examine the structural interaction between MCs and rNSCs, we injected AAV carrying CaMKII-driven mCherry (AAV-CaMKII-mCherry) into the hilus of Nestin-GFP mice to label excitatory neurons and found that the majority of mCherry-labeled cells are dentate GCs and hilar MCs, along with some CA3c pyramidal cells (Figures 1A and 1B). Since GCs and pyramidal cells do not project to the contralateral DG (Hsu et al., 2016), we limited our structural and functional analyses to the contralateral side for specificity. Within the hilus, injection of AAV-CaMKII-mCherry labeled ~82% of GluR2/3$^+$ cells (specific marker for MCs) and ~94% of AAV-CaMKII-mCherry-labeled cells were positive for GluR2/3 (Figures 1C and 1D), thus validating the efficiency and specificity of CaMKII-driven AAVs for targeting MCs. We next examined whether direct morphological associations exist between MC commissural projections and rNSCs. Confocal imaging of contralateral brain sections from Nestin-GFP mice unilaterally injected with AAV-CaMKII-mCherry revealed close associations between MC commissural IML projections and distal thin processes of GFP$^+$ rNSCs (Figure 1E). We further examined MC commissural projections and the distal processes of the rNSCs using serial section immuno-electron microscopy (Immuno-EM). We found that rNSC processes extended into the IML and ensheathed excitatory synapses between MC commissural axons and GCs (Figures 1F–1Q; Videos S1, S2, and S3). This is consistent with the concept that MCs directly mediate tonic glutamatergic signaling onto rNSCs. Additionally, immunogold labeling revealed NMDA receptor (NMDAR) NR1 subunits in the perisynaptic processes of rNSC in the IML (Figure S1; Video S4). These data provide high-resolution structural support for a direct glutamatergic MC-rNSC pathway. MCs also interact with several distinct types of dentate GABAergic interneurons (Hsu et al., 2016; Scharfman, 1995). It is possible that there is a substantial disynaptic GABAergic pathway onto the rNSCs. To examine the indirect association of MC commissural projections with rNSCs via dentate GABA interneurons, we injected AAV-CaMKII-eGFP into one DG for labeling MCs and AAV-hSyn-DIO-mCherry into the opposite DG to label local GABA interneurons using VGAT-Cre mice (Figure 1R). Confocal microscopy showed that MC commissural hilar projections closely associated with somas of dentate GABAergic interneurons (Figure 1R). Contralateral MC axons were further immunostained and imaged by electron microscopy. In the hilus, MC axons formed asymmetric (putatively glutamatergic) synapses

Figure 1. MC Commissural Projections Structurally Interact with rNSCs through Both Direct Glutamatergic and Indirect GABAergic Pathways

(A) Unilateral injection scheme for labeling MCs and contralateral analysis.

(B) Confocal image of mCherry expression at injection and contralateral DGs in a Nestin-GFP mouse. Scale bar, 100 μm.

(C) mCherry and GluR2/3 expression at injected DG. Arrowheads indicate colocalization. Scale bar, 20 μm.

(D) Efficiency and specificity of viral labeling of MCs.

(E) Close association of MC commissural projections (red) and rNSC bushy process (green) in the IML of the contralateral DG; boxed area shown on right. Scale bars, 50 μm (left) and 10 μm (right).

(F–Q) MC commissural axon terminals and synaptic contacts with GCs are directly ensheathed by Nestin-GFP$^+$ NSC processes.

(F1–F3) Bright-field micrograph of DAB-labeled rNSCs from a Nestin-GFP mouse (F1). Arrow region is shown at higher magnification in (F2) and (F3). rNSC processes reach the IML and intersect with CAMKII-GFP$^+$ axons of MCs (punctate DAB labeling). Scale bars, 200, 20, and 5 μm.

(G–I) 3D reconstruction of rNSC processes (green) traced from serial EM sections (G). Scale bars, 1 μm. Warm colors (H and I) depict axons embedded within large NSC process (purple/orange are DAB$^+$; see Video S1).

(J) EM section (J1, colored; J2, non-colored) from 3D reconstruction (arrows indicate penetrating axons). Scale bars, 0.5 μm. Green, rNSC; purple/orange, axons.

(K and L) 3D reconstructions of rNSC processes directly apposed (arrows) to synapses formed by MC axons (orange/purple) and GC dendritic spines (blue; see Videos S2 and S3). Scale bars, 2 μm.

(M) EM section of asymmetrical (putatively excitatory) synapse at MC axon terminals (orange in M1; black arrow in M2) with GC spines (light blue in M1; arrowhead in M2). Other MC axons are also visible (purple in M1; gray arrow in M2). Scale bar, 0.5 μm.

(N and O) Consecutive EM sections of rNSC processes (green; N1) associating with an asymmetrical synapse between MC axon (purple in N1 and O1; gray arrows in N2 and O2) and GC dendrite (dark blue in N1 and O1) and spine head (gray arrowhead in N2 and O2). Scale bars, 0.5 μm.

(P and Q) rNSC processes (green) at the GCL-IML border also directly appose unlabeled axon terminals. (P) Asymmetric synapse (red) with a spine head (blue). (Q) Asymmetrical synapse (yellow) with GC soma (blue). Scale bars, 0.5 μm.

(R) Viral injection scheme (top) in VGAT-Cre mice and confocal images (below) of MC contralateral hilar projections (green) associating with VGAT$^+$ interneuron soma (red). Boxed area shown on right. Scale bars, 100 and 10 μm.

(S–V) EM of asymmetric synapses from immunolabeled (dark) MC axon terminals in the contralateral hilus. (S and T) MC axo-dendritic synapses with dendrite (den); asterisks: additional asymmetric synapses from non-labeled axon terminals. (S′ and T′) Higher-magnification insets. (U and V) MC axo-spinous synapses with spines (sp). Scale bars, 1 μm (S and T) and 1.5 μm (S′–V).

(W) Slight hyperpolarization of GFP$^+$ rNSCs to muscimol (in TTX).

(X) Brief 50 μL spike of glutamate depolarized GFP$^+$ rNSCs (in TTX).

(Y) Illustration of rNSC regulation by MCs through direct glutamatergic and indirect GABAergic pathways.

See also Figure S1.

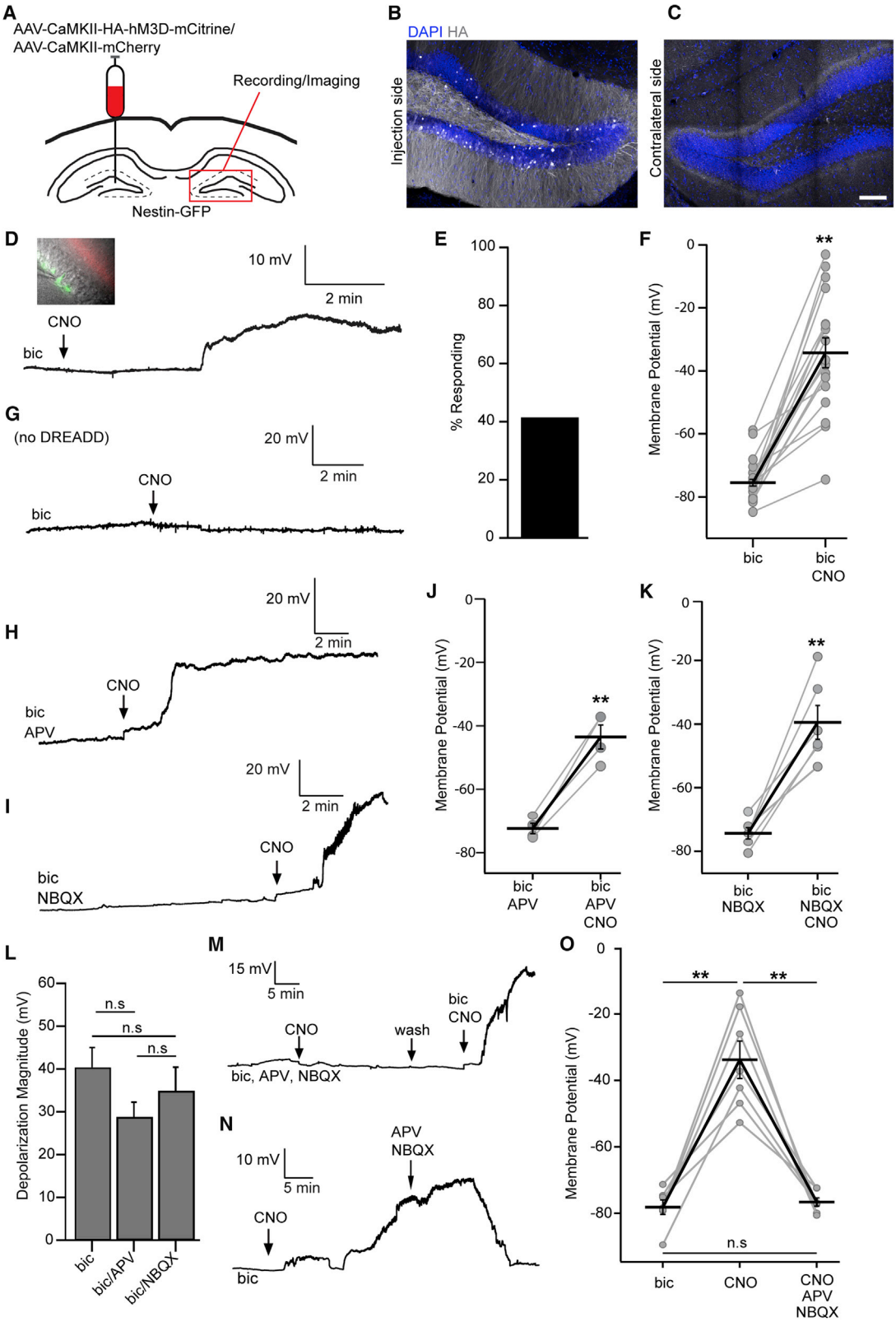

(legend on next page)

directly on dendrites. These dendrites received multiple inputs from non-labeled asymmetric axons (Figures 1S, 1S′, 1T, and 1T′), which are typical features of parvalbumin (PV)-expressing basket cell dendrites (Ribak and Seress, 1983). MC axons were also found to synapse with hilar dendritic spines, suggestive of non-basket cell interneurons (Figures 1U and 1V). These results thus provide morphological support for an indirect GABAergic pathway. While rNSCs do not possess synapses and typically exhibit hyperpolarized membrane potentials (Vm), single-cell analysis has detected mRNAs for both GABA and glutamate receptors (Shin et al., 2015). In order to determine whether these receptors are functional in rNSCs, which could potentially mediate both direct and indirect pathways onto rNSCs, we recorded Vm from Nestin-GFP$^+$ rNSCs in response to bath application of glutamate or muscimol ($GABA_A$ receptor agonist). Interestingly, in the presence of TTX, bath application of muscimol hyperpolarized rNSCs (Figure 1W), while bath application of glutamate depolarized rNSCs (Figure 1X). Taken together, our morphological data and electrophysiological recordings suggest that rNSCs are regulated by both glutamatergic and GABAergic signaling, potentially mediated by MC direct and indirect pathways, respectively (Figure 1Y).

MC Commissural Projections Functionally Interact with rNSCs through Both Direct Glutamatergic and Indirect GABAergic Pathways

To examine the functional interaction between MCs and rNSCs, we unilaterally injected a mixture of AAV carrying CaMKII-driven excitatory DREADDs (AAV-CaMKII-HA-hM3Dq-mCitrine) and AAV carrying CaMKII-driven mCherry (AAV-CaMKII-mCherry) into the hilus of Nestin-GFP mice and recorded Vm from contralateral GFP$^+$ rNSCs upon chemogenetic activation of MC commissural projections (Figure 2A; Figure S2A). Co-injecting two viruses facilitated the identification of MC commissural projections for electrophysiological recording, as mCitrine was not readily visualized by our fluorescence microscope. MC commissural projections at the contralateral side were detected 14 days after viral injection using immunostaining against the hemagglutinin (HA) tag (Figures 2B and 2C), indicating that hM3Dq was efficiently transported to the contralateral terminals.

We then dissected the functional effects of MC-mediated direct and indirect pathways on the Vm of the rNSCs. We first examined the MC direct pathway onto rNSCs. We recorded GFP$^+$ rNSCs upon chemogenetic activation of MC commissural projections in the presence of $GABA_A$ receptor blocker bicuculline in order to uncover potential glutamatergic components. Strikingly, we observed a significant depolarization in 41% of rNSCs ranging from 10 to 50 mV upon bath application of clozapine *N*-oxide (CNO) to activate MC commissural projections (Figures 2D–2F). This depolarizing effect was not observed in the GFP$^+$ rNSCs from non-viral-injected mice in the presence of bicuculline and CNO (Figure 2G), confirming that CNO by itself did not influence the Vm of the rNSCs. The highly variable depolarizing responses from rNSCs highlight a heterogeneity of rNSCs. Morphological heterogeneity in the height of rNSCs primary radial process has been recently reported (Gebara et al., 2016). Since MCs project axons to a specific molecular layer domain (Figures 1B, 1E, and 2C), we examined the reach of rNSCs into the IML and found that ~35% of the rNSCs reach MC projections (Figures S2B and S2C).

Next, we dissected the glutamate receptor subtypes mediating MC-induced rNSC depolarization. Recent single-cell RNA-sequencing data revealed AMPA receptor (AMPAR) and NMDAR expression in rNSCs (Shin et al., 2015); therefore, we recorded GFP$^+$ rNSCs upon bath application of CNO in the presence of bicuculline and NMDAR blocker APV or AMPAR blocker NBQX. Interestingly, we found that rNSCs still depolarized upon adding CNO despite NMDAR (Figures 2H and 2J) or AMPAR (Figures 2I and 2K) blockade, and the depolarization magnitude was not significantly different from bicuculline-only conditions (Figure 2L). These results suggest that NMDARs and AMPARs have redundant functions in mediating MC-induced rNSC depolarization. Furthermore, we addressed whether combined NMDA and AMPA components mediate MC-induced rNSC depolarization with two sets of experiments. First, we recorded rNSCs upon adding CNO in the presence of both APV and NBQX along with bicuculline and did not observe rNSC depolarization; however, after washing both glutamate blockers away, CNO-mediated rNSC depolarization was regained (Figures 2M and 2O). Second, we added CNO first to induce rNSC depolarization, which was later abolished upon adding glutamate receptor blockers (Figures 2N and 2O). Together, these data support the combined involvement of both AMPARs and NMDARs in mediating MC-induced rNSC depolarization.

To validate the chemogenetic manipulation, we also recorded the Vm of rNSCs upon optogenetic stimulation of MC

Figure 2. MC Commissural Projections Provide Direct Glutamatergic Inputs onto rNSCs

(A) Unilateral AAV injection scheme in the DG of Nestin-GFP mice for chemogenetic activation of MCs.

(B and C) HA$^+$ MCs at injection side (B) and commissural projection (C). Scale bar, 100 μm.

(D) Inset: whole-cell patch configuration from GFP$^+$ rNSC with red commissural projection. Below: depolarization of GFP$^+$ rNSC under $GABA_A$R blockade (bicuculline) upon CNO application.

(E) Percent of rNSCs that responded (≥10 mV) to chemogenetic activation of MC commissural projections.

(F) Membrane potentials before and during CNO in responding GFP$^+$ rNSCs (n = 17 cells, 15 mice, paired Student's t test).

(G) No membrane potential change from mice without viral injection.

(H and I) Depolarization of GFP$^+$ rNSCs in APV (H) or NBQX (I). Bicuculline was present in both conditions.

(J and K) Summary of rNSC depolarization in NMDAR blockade (J; n = 4 cells, 3 mice) or AMPAR blockade (K; n = 6 cells, 3 mice). Paired Student's t tests.

(L) Comparison of rNSC depolarization in AMPAR or NMDAR blockade (n = 17, 4, 6 cells; 15, 3, 3 mice).

(M) Combined blockade of NMDARs and AMPARs (APV and NBQX) in responding rNSCs.

(N) rNSC depolarization was abolished upon bath application of APV and NBQX.

(O) Membrane potentials under combined AMPAR and NMDAR blockade in responding rNSCs (n = 7 cells, 5 mice).

Values represent mean ± SEM. Significance was determined based on $p < 0.05$ (n.s: $p > 0.05$; *$p < 0.05$; **$p < 0.01$). See also Figure S2.

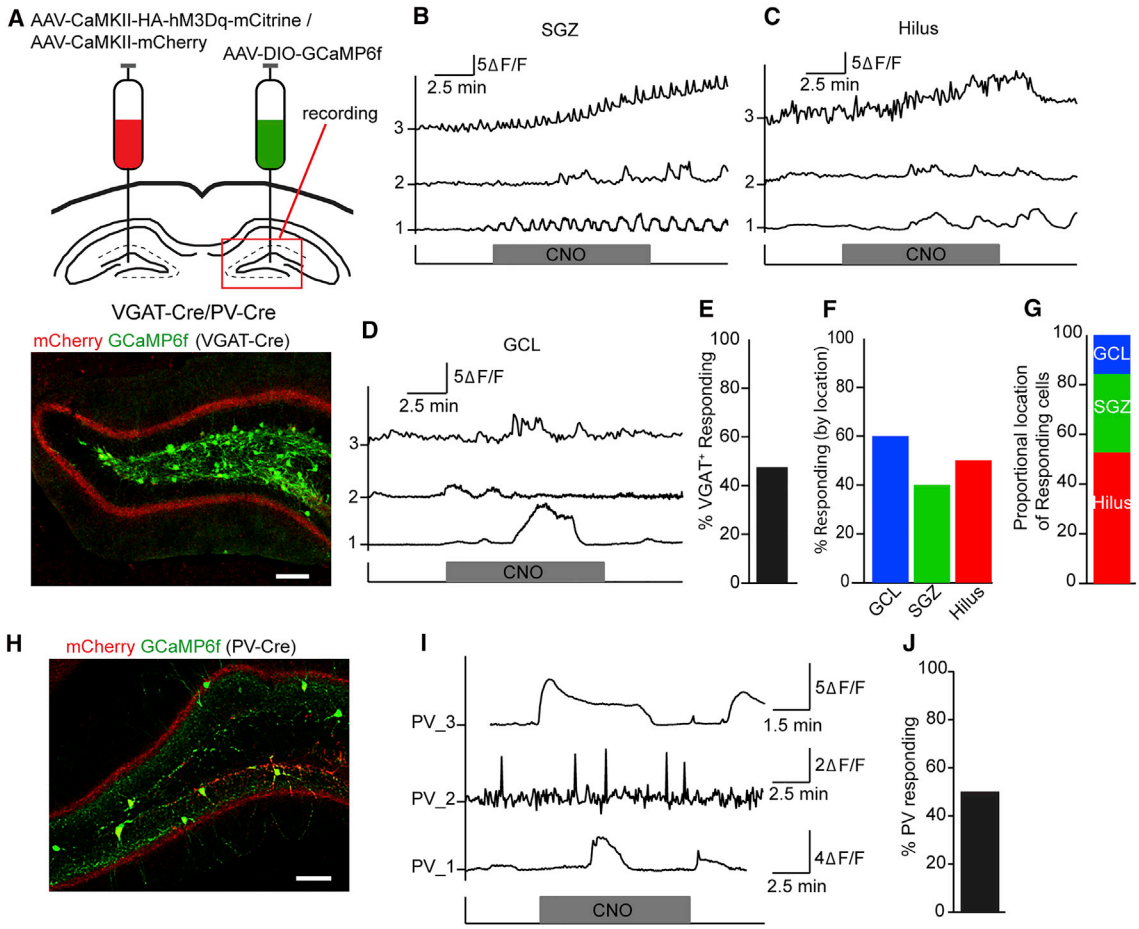

Figure 3. MC Commissural Projections Excite a Subset of Dentate GABA Interneurons

(A) Top: viral injection scheme in VGAT-Cre (or PV-Cre) mice. Bottom: commissural projections and GCaMP6f expression in the contralateral DG of a VGAT-Cre mouse. Scale bar, 100 μm.

(B–D) Representative ΔF/F signals in contralateral VGAT$^+$ interneurons from subgranular zone (SGZ) (B), hilus (C), or granule cell layer (GCL) (D) upon CNO application.

(E) Percent of GCaMP6f$^+$ GABA interneurons that increased Ca^{2+} events (≥50%) upon chemogenetic activation of MC commissural projections.

(F) Percent of responsive VGAT$^+$ cells residing within SGZ, hilus, or GCL.

(G) Distribution of the responders among the SGZ, hilus, and GCL.

(H) Commissural projections and GCaMP6f expression in the contralateral DG of a PV-Cre mouse. Scale bar, 100 μm.

(I) Representative ΔF/F signals in contralateral PV$^+$ interneurons upon CNO application.

(J) Percent of GCaMP6f$^+$ PV interneurons that increased Ca^{2+} events (≥50%) in response to chemogenetic activation of MC commissural projections.

commissural projections in contralateral brain slices prepared from Nestin-GFP mice injected with AAV-CaMKII-ChR2-mCherry (Figure S2D). We recorded in the presence of $GABA_A$ receptor blocker bicuculline to uncover the glutamatergic component. Consistent with depolarization of rNSCs induced by chemogenetic activation of MCs, we observed light-evoked depolarization of rNSCs in response to optogenetic activation of MC commissural projections (Figure S2E). Though the depolarization amplitude appeared small and the kinetics were slow, the responses were phase-locked to the light delivery onto the MC commissural projections. To enhance the reliability of light-evoked responses in rNSCs, we added low-concentration K^+ channel blocker 4-AP (Grubb and Burrone, 2010). Indeed, this resulted in reliable, robust depolarization in rNSCs upon blue light stimulations (Figures S2F and S2G). Thus, both chemogenetic and optogenetic approaches confirm a glutamatergic direct pathway onto rNSCs.

Since local GABAergic interneurons regulate quiescence of rNSCs (Song et al., 2012), we next examined the plausibility of an indirect MC-GABAergic pathway regulating rNSCs. To probe the functional role of the MC commissural pathway in exciting local GABA interneurons, we injected a mixture of AAV-CaMKII-HA-hM3Dq-mCitrine and AAV-CaMKII-mCherry to one DG to label MCs and a Cre-dependent calcium sensor AAV-DIO-GCaMP6 to the other DG to label GABA cells using VGAT-Cre mice (Figure 3A). We examined calcium signals of dentate GABA interneurons in response to chemogenetic activation of MC commissural projections by bath application of CNO and

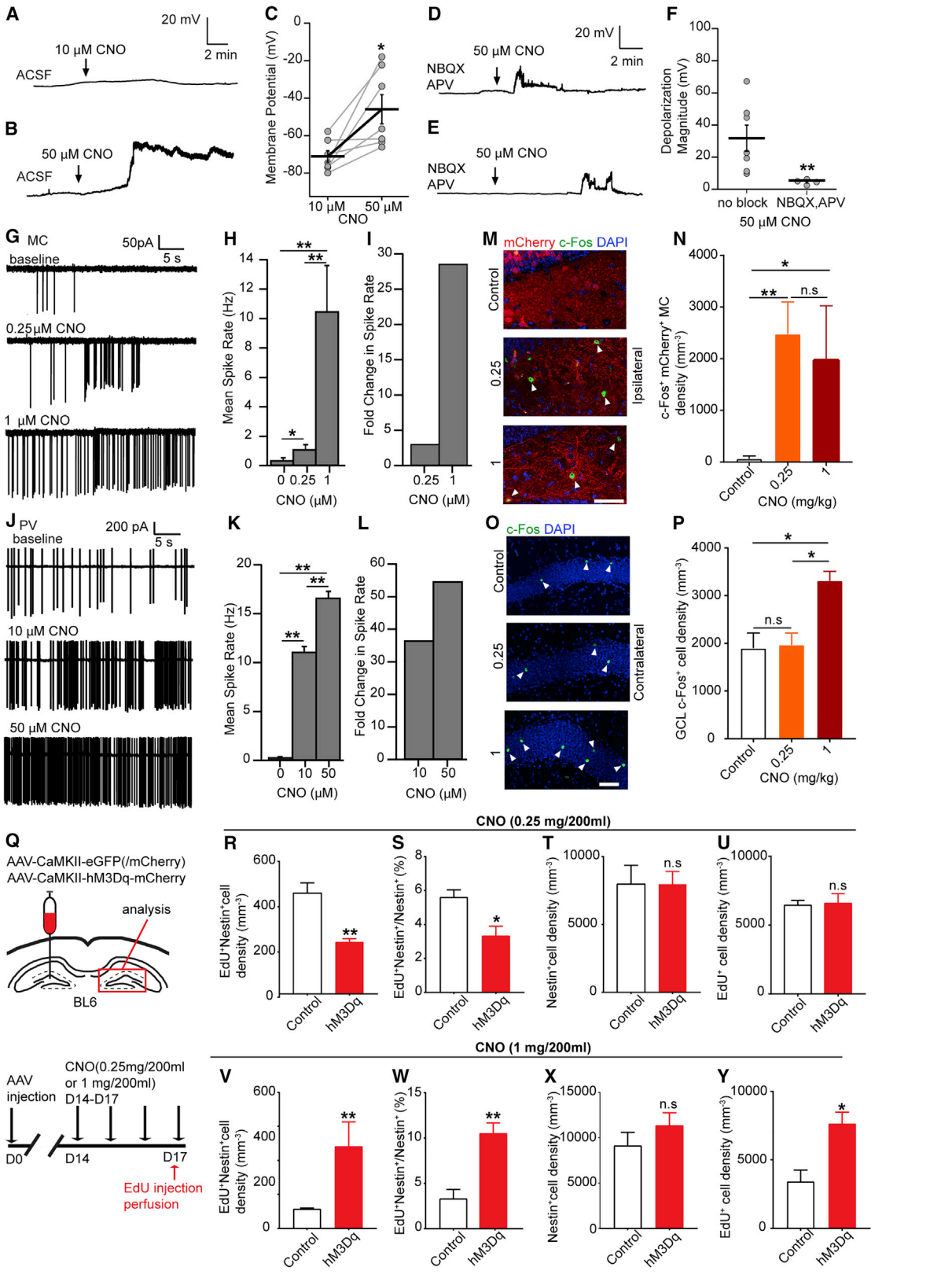

(legend on next page)

observed a significant increase of Ca^{2+} signals in 48% of GABA interneurons located at the subgranular zone (SGZ; 40% responding), hilus (50% responding), and granule cell layer (GCL; 60% responding) upon CNO application (Figures 3B–3F), suggesting that activation of MC commissural projections excites local GABA interneurons. Interestingly, CNO-induced responses in dentate GABA neurons were highly heterogeneous (Figures 3B–3D), consistent with the recent finding that the MC commissural pathway preferentially recruits several subsets of dentate GABA interneurons (Hsu et al., 2016). Dentate PV interneurons can functionally interact with and regulate rNSCs (Song et al., 2012), and our Ca^{2+} imaging showed that 32% of the responding cells were from the SGZ, where PV basket cells reside (Figure 3G). Therefore, we hypothesized that PV basket cells in part mediate the MC GABAergic indirect pathway onto rNSCs. To probe the functional role of the MC commissural pathway in regulating PV excitability, we repeated the same injections in PV-Cre mice (as for VGAT-Cre; Figure 3H) and observed a significant increase in the Ca^{2+} signals in 50% of PV interneurons upon CNO (Figures 3I and 3J), suggesting that PV interneurons in part mediate the MC GABAergic indirect pathway onto rNSCs.

rNSC Quiescence Is Differentially Regulated by Distinct MC Activation States

The presence of direct and indirect pathways onto rNSCs raised a question of the net effects of MC commissural projections on rNSCs under different MC activation states. The extent of neuronal activation using chemogenetic approaches is typically CNO dose dependent (Sternson and Roth, 2014). We first examined rNSCs in acute brain slices prepared from adult Nestin-GFP mice injected with CaMKII-hM3Dq by recording the GFP^+ rNSCs using CNO concentrations of 10 and 50 μM to represent moderate and high activation states of MCs. We recorded rNSCs in the absence of the GABA and glutamate receptor blockers to reflect the natural states of the circuit. We found that 10 μM CNO did not induce significant changes in the Vm of the rNSCs (Figures 4A and 4C); in contrast, 50 μM CNO induced significant depolarization in rNSCs (Figures 4B and 4C). Furthermore, the high-concentration CNO-induced depolarization was abolished in the presence of AMPAR and NMDAR blockers (Figures 4D–4F), suggesting that ionotropic glutamate receptors mediate membrane depolarization in rNSCs during high MC activation. Interestingly, we occasionally observed rapid depolarizing membrane potential transients during the bath application of 50 μM CNO in the presence of AMPA and NMDA blockers (Figures 4D and 4E), which is in sharp contrast to the prolonged depolarization without the AMPA and NMDA blockers (Figure 4B), suggesting the potential involvement of other MC-induced niche signals onto rNSCs under the high MC activation state. Importantly, these membrane transients did not affect the overall Vm of the rNSCs. Together, these results suggest a switch from indirect pathway dominance at moderate MC activation state (low-dose CNO) to direct pathway dominance at high MC activation state (high-dose CNO).

To examine the circuit mechanism underlying this switch, we performed Ca^{2+} imaging and electrophysiology in acute slices to address dose-dependent effects of CNO on MCs and PV cells. Our Ca^{2+} imaging analysis revealed a significant increase in MCs that responded to high CNO concentrations (Figures S3A and S3B) as well as a trend of CNO dose dependence (Figure S3C). Calcium imaging provided a quick readout for MC activity upon chemogenetic activation, but to get a more precise measurement of MC firing rates, we performed cell-attached electrophysiology recording. We observed a significant increase of MC firing at both low- and high-dose CNO as compared to baseline (Figures 4G–4I). Importantly, the increase of MC firing rate was dose dependent. Next, we performed cell-attached recording in dentate PV cells upon various CNO doses to address CNO dose-dependent effects on the indirect pathway. Similarly, we observed a significant increase of PV firing rate at both low- and high-dose CNO as compared to the baseline, and the increase of PV firing rate was dose dependent (Figures 4J–4L). From our slice recording, it appears that PV cells have a higher basal firing rate than MCs (Figures 4G and 4J). Interestingly, low-dose CNO increased MC and PV firing rates by 3- and 37-fold, respectively (Figures 4I and 4L), compared to the baselines. In contrast, high-dose CNO increased MC and PV firing rates by 28- and 55-fold, respectively (Figures 4I and 4L).

Figure 4. rNSC Quiescence Is Differentially Regulated by Distinct MC Activation States

(A and B) Whole-cell recordings of rNSCs at low-dose (A) and high-dose (B) CNO in the absence of blockers.
(C) rNSC membrane potentials upon adding 10 and 50 μM CNO (n = 7 cells, 4 mice; paired Student's t test).
(D and E) Membrane depolarizations were blocked by AMPAR antagonist NBQX (D) and NMDAR antagonist APV (E).
(F) Depolarization magnitude of rNSCs in glutamate receptor blockers upon CNO (n = 7 cells from 3 mice with no blockers and 4 cells from 3 mice with blockers; Wilcoxon rank test).
(G) hM3Dq-$mCherry^+$ MC spiking activity at indicated CNO concentrations (in bicuculline, NBQX, and APV).
(H) Representative CNO dose-dependent spike frequency in hM3Dq-$mCherry^+$ MCs (n = 25,19,3 sweeps; Wilcoxon rank test).
(I) Fold change in MC spike rate relative to baseline.
(J) Contralateral PV spiking activity at indicated concentrations of CNO (no blockers).
(K) Representative CNO dose-dependent spike frequency in contralateral PV^+ interneurons. (n = 25, 20, 20 sweeps; Wilcoxon rank test).
(L) Fold change in PV spike rate relative to baseline.
(M) c-Fos^+ $mCherry^+$ MCs (arrowheads) in hM3Dq-mCherry- or mCherry-injected DGs in control, low-, and high-dose CNO. Scale bar, 50 μm.
(N) Density of c-Fos^+ $mCherry^+$ MCs (n = 3 mice in each group).
(O) c-Fos^+ cells (arrowheads) in contralateral DGs. Scale bar, 50 μm.
(P) Density of GCL c-Fos^+ cells at the contralateral DG (n = 3 mice in each group).
(Q) Viral injection scheme and experimental paradigm for *in vivo* chemogenetic activation of MCs.
(R–U) Density and percentage of activated rNSCs (R and S), $Nestin^+$ rNSC pool (T), and EdU^+ cell density (U) at the low-dose CNO (n = 3, 5 mice in each group).
(V–Y) Density and percentage of activated rNSCs (V and W), $Nestin^+$ rNSC pool (X), and EdU^+ cell density (Y) at the high-dose CNO (n = 3, 4 mice in each group).
Values represent mean ± SEM. Significance was determined based on $p < 0.05$ (n.s: $p > 0.05$; *$p < 0.05$; **$p < 0.01$). See also Figure S3.

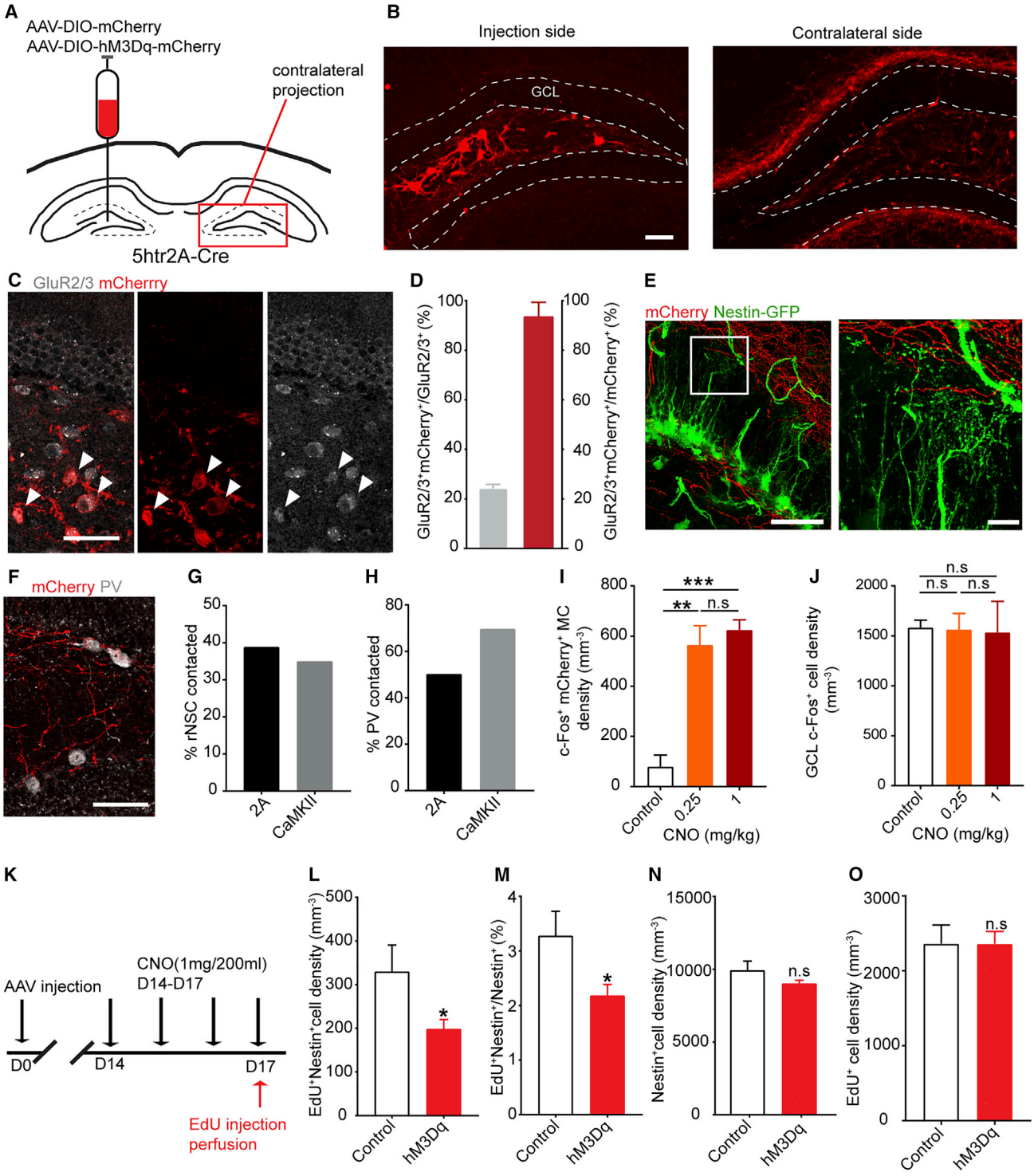

Figure 5. Sparse Activation of MC Inputs Promotes NSC Quiescence

(A) Viral injection scheme in 5htr2A-Cre mice.

(B) Selective labeling of MCs and commissural projections by AAV-DIO-mCherry. Scale bar, 50 μm.

(C) mCherry labeled a small subset of GluR2/3$^+$ MCs (white) in the hilus. Arrowheads indicate colocalization. Scale bar, 50 μm.

(D) mCherry$^+$GluR2/3$^+$ cells showed specificity for MCs but only labeled a subset of MCs.

(E) 5htr2A-MC commissural projections (red) formed close associations with the bushy processes of rNSCs (green); expanded view of boxed area is shown on right. Scale bars, 50 μm (left), 10 μm (right).

(legend continued on next page)

Together, these results reveal a differential regulation of MC and PV responses to low- and high-dose CNO: low-dose CNO increased the firing rate of PV cells 12 times that of the increase in MCs, while high-dose CNO increased the firing rate of PV cells only 2 times that of the increase in MCs. These results thus suggest that the indirect pathway is more sensitive to low-dose CNO treatment, which subsequently leads to more pronounced interneuron firing and GABA release. Together, these results provide mechanistic insights into the switch from indirect pathway dominance to direct pathway dominance at high-dose CNO.

To address the *in vivo* effects of CNO dose-dependent MC activation, we performed c-Fos staining at both ipsilateral and contralateral DGs in wild-type (WT) mice injected with AAV-CaMKII-hM3Dq. At the ipsilateral side, we quantified c-Fos$^+$ MC somas, while at contralateral side, we quantified c-Fos$^+$ dentate GCs. Interestingly, we observed that low- and high-dose CNO similarly increased the density of c-Fos$^+$ MCs at the ipsilateral side (Figures 4M and 4N), but only high-dose CNO induced a significant increase of the density of c-Fos$^+$ cells in the contralateral GCL (Figures 4O and 4P). Additionally, high-dose CNO did not significantly alter the distribution of the c-Fos$^+$ GCs within the GCL between control and hM3Dq groups (Figure S3D). These results suggest that though both CNO doses induced MC activation, only high-dose CNO induced sufficient glutamate release to excite contralateral GCs and rNSCs.

To probe the function of MCs in regulating rNSCs *in vivo*, we administered low- or high-dose CNO drinking water (0.25 or 1 mg/200 mL) in C57BL6 mice injected with control AAV-CaMKII-eGFP (or AAV-CaMKII-mCherry) or excitatory DREADDs AAV-CaMKII-hM3Dq-mCherry for 4 days, followed by thymidine analog EdU injections on the last day to label the proliferating cells (Figure 4Q). Activated rNSCs were identified as contralateral SGZ cells with Nestin$^+$ radial processes and EdU incorporation (Figure S3E). Stereological analysis showed that chemogenetic activation of MCs at low-dose CNO led to a significant decrease in the density (Figure 4R) and percentage (Figure 4S) of activated rNSCs, without significant alteration of the Nestin$^+$ rNSC pool (Figure 4T) or EdU$^+$ cell density (Figure 4U). In contrast, chemogenetic activation of MCs at high-dose CNO led to a significant increase in the density (Figure 4V) and percentage (Figure 4W) of activated rNSCs, along with a significant increase of the EdU$^+$ cell density (Figure 4Y), without significant alteration of the Nestin$^+$ rNSC pool (Figure 4X). Together, these results suggest that rNSC quiescence is differentially regulated by distinct MC activation states.

Since high MC activation induced by high CNO concentration may represent pathological conditions, we tested a naturalistic stimulation of MC activity. MCs are known to strongly respond to spatial exploration (Danielson et al., 2017). We therefore continuously exposed adult Nestin-GFP mice to enriched environment (EE) for 13 days. Compared to standard housing, EE increased the proportion of MCs that express c-Fos (Figures S3F and S3G) without changing the total number of MCs (Figure S3H). In contrast, EE did not alter the proportion of PV cells that express c-Fos (Figures S3I and S3J), indicating that EE may differentially activate MC and PV interneurons. Furthermore, this increase was accompanied by a 147% increase in the proportion of proliferating rNSCs (Figure S3K). Together, these results highlight the link between a high MC activation state in physiological conditions and rNSC behavior and suggest that EE favors the direct MC-rNSC pathway.

Sparse Activation of MC Inputs Promotes NSC Quiescence

Manipulating MC activity at moderate and high levels demonstrated that the strengths of MC-rNSC connections are important for the balance between direct and indirect pathways and, in turn, rNSC quiescence. However, the CaMKII promoter used for *in vivo* studies is not specific to the MCs, so driving these cells may introduce abnormal circuit effects within the ipsilateral DG. It has been historically difficult to selectively target only MCs. Two mouse lines, Crlr-Cre and Drd2-Cre, were reported to label MCs, but both labeled secondary or tertiary cell types besides MCs. (Gangarossa et al., 2012; Jinde et al., 2012; Puighermanal et al., 2015). A recent study using double fluorescence *in situ* hybridization demonstrated that 5ht2A receptors (5htr2A) colocalize with calretinin (Tanaka et al., 2012), another marker for MCs. To examine the specificity of 5htr2A-Cre mice in targeting MCs, we injected Cre-dependent AAV-expressing mCherry (AAV-DIO-mCherry) to the hilus of 5htr2A-Cre mice (Figure 5A). We observed prominent targeting of hilar cells with typical morphology of MCs (Figure 5B). The vast majority of mCherry$^+$ cells (94%) colocalized with MC-specific marker GluR2/3 (Figures 5C and 5D), suggesting that 5htr2A-Cre line specifically targets MCs. Notably, AAV-labeled 5htr2A-expressing MCs only represent 24% of the total GluR2/3$^+$ MC population (Figure 5D). Although the 5htr2A-Cre line appeared to more specifically label MCs than the two existing lines, we did notice that some CA3c pyramidal cells were labeled, similar to the Drd2-Cre mice with viral injection to the DG.

Since 5htr2A only labeled a subset of MCs, we addressed whether sparse MC inputs, which are believed to be more physiologically relevant, favor either the direct or the indirect pathway onto rNSCs. We first confirmed the efficacy of chemogenetic activation of 5htr2A-expressing MCs by co-injecting Cre-dependent GCaMP6 and hM3Dq-mCherry into 5htr2A-Cre mice and performing calcium imaging of 5htr2A-expressing MCs in acute

(F) 5htr2A-MC commissural projections (red) formed close associations with somas of contralateral PV$^+$ interneurons (white) in the SGZ. Scale bar, 50 μm.
(G and H) Percentage of contralateral rNSCs (G) or PV$^+$ interneurons (H) contacted by 5htr2A-MC or CaMKII-MC projections.
(I and J) Density of c-Fos$^+$mCherry$^+$ MCs at the injection side (I) or c-Fos$^+$ GCL cells in the contralateral DG (J) upon low- and high-dose CNO (n = 3 mice in each group).
(K) Experimental paradigm for *in vivo* chemogenetic activation of MCs.
(L–O) Density and percentage of activated rNSCs (L and M), Nestin$^+$ rNSC pool (N), and EdU$^+$ cell density (O) at the MC commissural projection side (n = 3 mice in control group and 5 mice in hM3Dq group).
Values represent mean ± SEM. Significance was determined based on $p < 0.05$ (n.s: $p > 0.05$; *$p < 0.05$; **$p < 0.01$, ***$p < 0.001$). See also Figure S4.

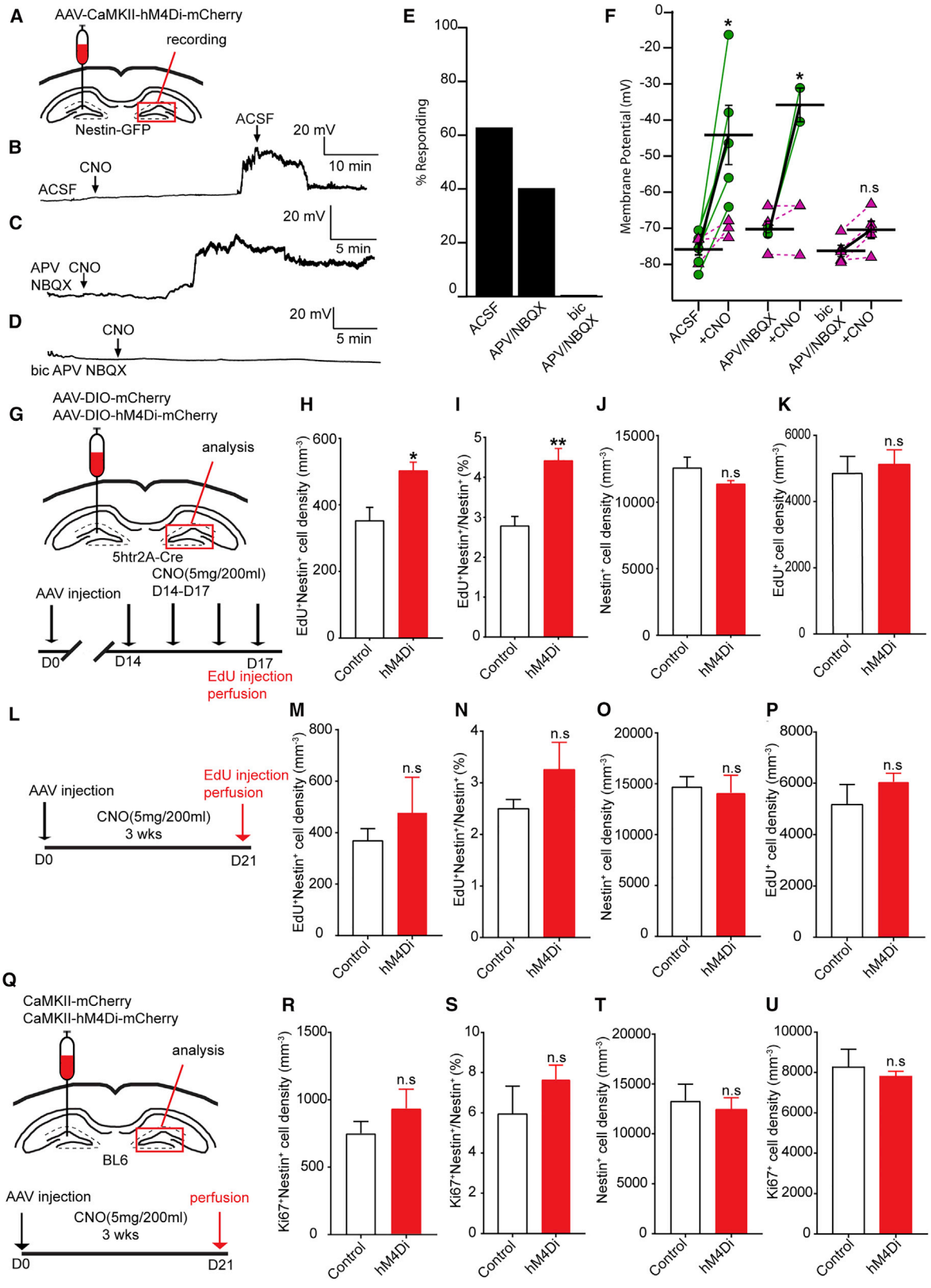

(legend on next page)

brain slices (Figures S4A and S4B). Chemogenetic activation of hM3Dq-mCherry$^+$GCaMP6$^+$ MCs led to CNO-induced calcium increases in 5htr2A-expressing MCs (Figure S4C). CNO-induced responses in 5htr2A-expressing MCs were variable (Figure S4C), in agreement with observed functional heterogeneity in MCs (GoodSmith et al., 2017). These experiments validate the specificity of the 5htr2A-Cre line in targeting MCs and the efficacy of CNO-induced chemogenetic activation of MCs.

Next, we examined whether morphological associations exist between 5htr2A-Cre-MC projections and rNSCs or dentate PV cells. We found that 5htr2A-Cre-MC projections similarly associated with rNSCs and PV cells (as the CaMKII-MC projections; Figures 5E and 5F). Furthermore, we quantified and compared the percentage of rNSCs (out of all rNSCs) and PV cells (out of all PV cells) that contacted 5htr2A-Cre-MC or CaMKII-MC projections. We found a similar percentage of rNSCs reaching 5htr2A-Cre-MC projections (Figure 5G) as compared to CaMKII-MC projections (38% for 2A, 35% for CaMKII), but a smaller percentage of PV cells associated with 5htr2A-Cre-MC projections (Figure 5H) as compared to CaMKII-MC projections (50% for 2A, 70% for CaMKII). In addition, CaMKII-MC projections are much more abundant in the hilus and IML than 5htr2A-Cre-MC projections (Figures 1E, 1R, 5E, and 5F). These morphological data suggest that both CaMKII-MC and 5htr2A-Cre-MC projections interact with a subset of rNSCs and PV cells; however, CaMKII-MC projections are more abundant. To determine the CNO dose-dependent activation state of MCs *in vivo*, we performed c-Fos staining in 5htr2A-Cre mice injected with AAV-DIO-hM3Dq at low- and high-dose CNO (0.25 and 1 mg/200 mL, respectively). As a result, we observed that low- and high-dose CNO similarly increased the density of c-Fos$^+$ MCs at the ipsilateral side, thus confirming MC activation in response to CNO administration (Figure 5I). Interestingly, in contrast to differential c-Fos expression at the contralateral side with low- and high-dose CNO in WT mice (with CaMKII-hM3Dq labeled MCs), we did not observe significant difference in 5htr2A-Cre mice (Figure 5J), suggesting that moderate and high MC activation states induced similar circuit effects in 5htr2A-Cre mice. Together, the morphological and functional data suggest that CaMKII-MC projections provide more glutamate to rNSCs and local interneurons as compared to 5htr2A-Cre-MC projections; therefore, MCs in 5htr2A-Cre mice need to be driven harder in order to supply the same amount of GABA and glutamate for rNSCs as that of CaMKII-MC projections.

We then addressed the functional effects of sparse MC activation on rNSCs *in vivo*. Since we did not observe significant difference in circuit effects induced by low- and high-dose CNO, we utilized high-dose CNO to selectively activate 5htr2A-expressing MCs into a high activation state and examined rNSC quiescence after 4-day administration of the high-dose CNO in the drinking water (1 mg/200 mL) (Figure 5K). Our stereological analysis showed that chemogenetic activation of MCs significantly decreased the density and percentage of activated rNSCs (Figures 5L and 5M) at the contralateral DG compared to the sham treatment group without altering the Nestin$^+$ rNSC pool (Figure 5N) or EdU$^+$ cell density (Figure 5O). These results suggest that sparse MC-rNSC connections remained indirect pathway dominant even when driven at high strength.

Taken together, these results suggest that MC-mediated glutamatergic and GABAergic signaling onto rNSCs determines the balance between direct and indirect pathways. When MC activation is moderate, such as might occur under physiological conditions, the indirect pathway is dominant; when MC activation is high, such as might occur under highly salient or pathological conditions, the direct pathway becomes dominant.

Inhibition of MCs Leads to Significant Depolarization and Increased Activation of the rNSCs through the Indirect Pathway

It is unclear whether indirect pathway dominance in rNSC regulation could persist without excitatory drive from MC hilar projections. We therefore addressed whether a ''loss of function'' in MC commissural projections would still favor indirect GABAergic pathway dominance in the regulation of rNSCs. We first performed slice electrophysiology to address the effect of chemogenetic inhibition of MCs on the Vm of the rNSCs using inhibitory DREADDs (hM4Di). Unilateral injections of AAV-CaMKII-hM4Di-mCherry were made in Nestin-GFP mice for chemogenetic inhibition of MCs, and electrophysiological recordings were made from contralateral GFP$^+$ rNSCs in the absence of receptor

Figure 6. Chemogenetic Inhibition of MCs Leads to Significant Depolarization and Increased Activation of the rNSCs through the Indirect Pathway

(A) Viral injection scheme in Nestin-GFP mice for electrophysiological recordings of rNSCs.

(B) Membrane depolarization in a GFP$^+$ rNSC upon chemogenetic MC inhibition in the absence of blockers. Note recovery upon washout of CNO.

(C) Depolarization arose even in the presence of glutamatergic receptor blockade (NBQX and APV).

(D) No change in membrane potential under both glutamatergic and GABAergic receptor blockade (bicuculline, NBQX, APV).

(E) Percent of responding rNSCs ($\geq$10 mV) with and without pharmacological blockade.

(F) Membrane potentials in response to chemogenetic inhibition of MC commissural projections. Green circles indicate responding rNSCs; purple triangles, non-responsive (n = 8, 5, 5 cells from 5, 3, 3 mice; Wilcoxon rank test).

(G) Viral injection scheme and experimental paradigm for chemogenetic inhibition of MCs in 5htr2A-Cre mice.

(H–K) Density and percentage of activated rNSCs (H and I), Nestin$^+$ rNSC pool (J), and EdU$^+$ cell density (K) at the MC commissural projection side for short-term analysis (n = 4 mice in each group).

(L) Experimental paradigm for long-term chemogenetic inhibition of MCs in the 5htr2A-Cre animal.

(M–P) Density and percentage of activated rNSCs (M and N), Nestin$^+$ rNSC pool (O), and EdU$^+$ cell density (P) at commissural projection side for long-term analysis in 5htr2A-Cre mice (n = 3 mice in each group).

(Q) Experimental paradigm for long-term chemogenetic inhibition of MCs using CaMKII-hM4Di in BL6 mice.

(R–U) Density and percentage of activated rNSCs (R and S), Nestin$^+$ rNSC pool (T), and Ki67$^+$ cell density (U) at the MC commissural projection side for long-term analysis in WT mice with CaMKII-labeled MCs (n = 3 mice in each group).

Values represent mean ± SEM. Significance was determined based on $p < 0.05$ (n.s: $p > 0.05$; *$p < 0.05$; **$p < 0.01$). See also Figure S5.

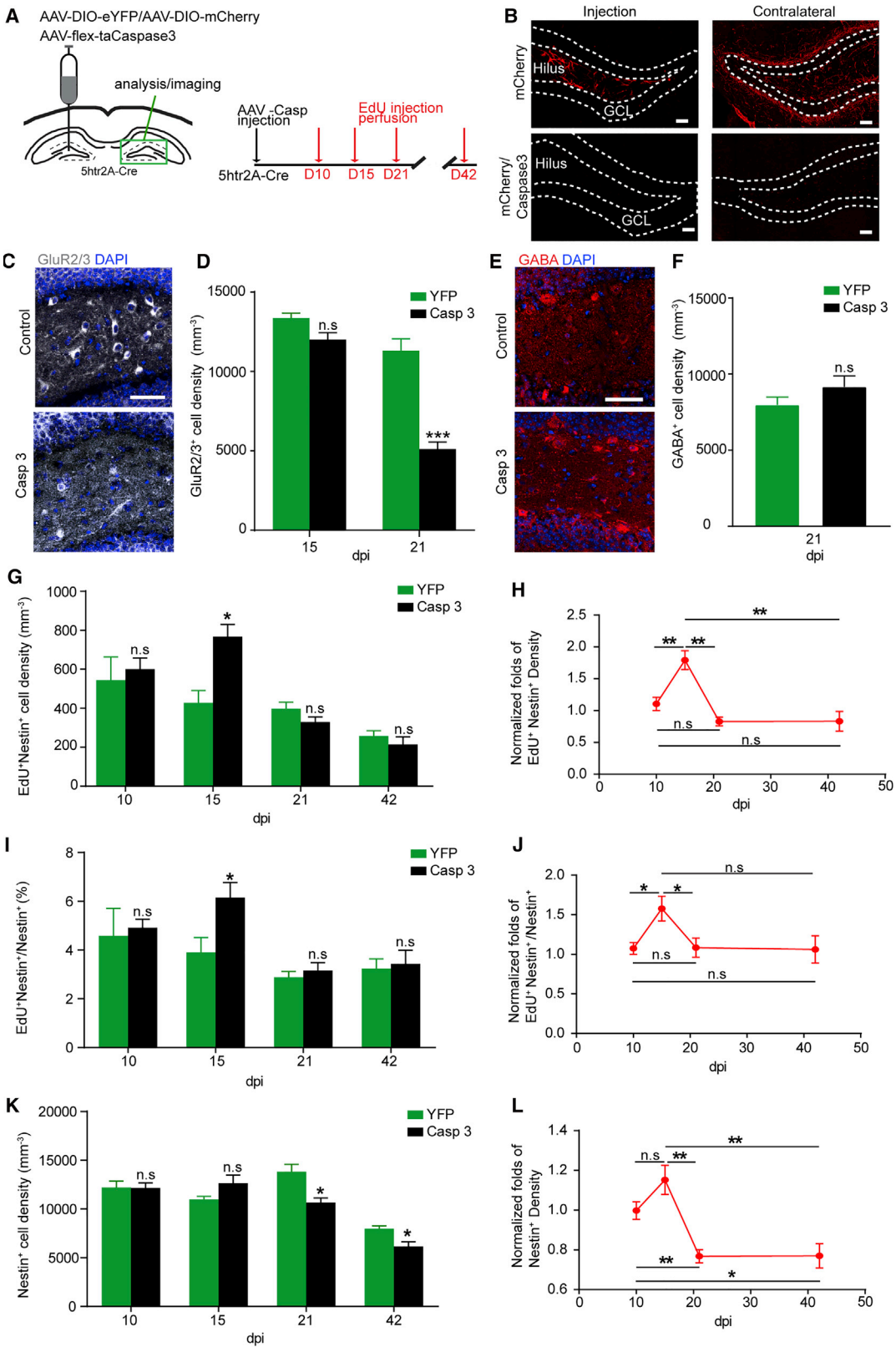

(legend on next page)

blockers (Figure 6A). Unexpectedly, we observed a significant depolarization in 60% of recorded rNSCs upon adding CNO for chemogenetic inhibition of MCs ranging from 25 to 60 mV (Figures 6B, 6E, and 6F).

Next, we addressed the circuit mechanisms underlying MC-inhibition-mediated rNSC regulation. We recorded rNSCs in the presence of glutamate receptor blockers (APV+NBQX) or combined GABA and glutamate receptor blockers (Bic+APV+NBQX). The goal of these experiments was to address the relative contribution of glutamatergic and GABAergic signaling in regulating rNSCs in the context of chemogenetic inhibition of MCs. Interestingly, we found that rNSCs depolarized in the presence of glutamate blockers (APV+NBQX) (Figures 6C, 6E, and 6F), but the rNSC depolarization was abolished in the presence of combined GABA and glutamate blockers (Figures 6D–6F). These results suggest that MC inhibition reduced both glutamatergic and GABAergic signaling onto rNSCs through direct and indirect pathways, respectively, but reduced GABA signaling from the indirect pathway contributes to rNSC depolarization, as blocking $GABA_A$ receptors (but not AMPARs and NMDARs) abolished the rNSC depolarization.

To probe the functional role of MC inhibition in rNSC regulation *in vivo*, we took a chemogenetic approach to inhibit MCs using hM4Di in 5htr2A-Cre mice. First, we performed Ca^{2+} imaging in acute brain slices prepared from 5htr2A-Cre mice co-injected with Cre-dependent GCaMP6 and hM4Di-mCherry to validate the efficacy of chemogenetic inhibition of MCs in the presence of CNO (Figure S5A). We observed that chemogenetic inhibition of hM4Di-mCherry$^+$ GCaMP6$^+$ co-labeled MCs abolished spontaneous calcium activity in MCs upon bath application of CNO (Figures S5B and S5C). Next, we induced inhibition of MCs for 4 days by administration of CNO in the drinking water (5 mg/200 mL) (Figure 6G). Interestingly, we observed a significant increase in the density and percentage of activated rNSCs (Figures 6H and 6I) without significant change in the Nestin$^+$ rNSC pool (Figure 6J) or EdU$^+$ cell density (Figure 6K), consistent with our observed MC-inhibition induced depolarization in rNSCs.

To address chronic effects of MC inhibition on rNSC maintenance, we performed long-term chemogenetic inhibition of MCs using inhibitory DREADD (hM4Di) by providing CNO water for 21 days in both 5htr2A-Cre mice that sparsely labeled MCs (Figure 6L) and WT mice with abundantly labeled MCs by CaMKII virus (Figure 6Q). Unexpectedly, we observed no significant changes in the rNSC pool in either 5htr2A-Cre or WT mice (Figures 6O and 6T), suggesting that chronic MC inhibition did not alter the rNSC pool despite widespread MCs inhibition. Additionally, we observed no significant change in density or percentage of activated rNSCs (Figures 6M–6N, 6R, and 6S) or EdU$^+$ (or Ki67$^+$) cell density (Figures 6P and 6U). It is likely that long-term inhibition of MCs induced circuit adaptation or DREADD receptor desensitization.

To provide further evidence of indirect pathway dominance in regulating rNSC quiescence upon MC inhibition, we selectively deleted glutamate receptors in rNSCs and examined whether glutamate signaling is required for rNSC quiescence. As our electrophysiology recordings identified that both AMPARs and NMDARs were required for depolarization of rNSCs mediated by the MC direct pathway, we selectively targeted three genes encoding AMPAR subunits (GluA1, -A2, and -A3) and the gene encoding the NMDAR GluN1 subunit for deletion with the *Gria1-3*$^{fl/fl}$*Grin1*$^{fl/fl}$ mice (Gu et al., 2016; Hutchison et al., 2018; Lu et al., 2013). To genetically remove both AMPARs and NMDARs in rNSCs, we crossed an inducible *Nestin-CreER*^{T2} mouse line (Kuo et al., 2006) with *Gria1-3*$^{fl/fl}$*Grin1*$^{fl/fl}$ mice to generate quintuple transgenic mice (*Nestin-CreER*$^{T2+/-}$ *Gria1-3*$^{fl/fl}$*Grin1*$^{fl/fl}$). The quadruple knockout mice eliminated concerns associated with glutamate receptor subunit compensation that occurs during only partial deletion (Adesnik et al., 2008; Lu et al., 2009) (Figure S5D). To induce high-level recombination in rNSCs and their progeny at the population level, we injected tamoxifen (TMX; 100 mg/kg) for 7 consecutive days, and mice were sacrificed 4 weeks after the last TMX induction following four EdU injections at the last day (Figure S5E). We then quantified the density of activated rNSCs, the activation percentage of rNSCs, and the size of the rNSC pool. Compared to control mice (genotype: *Gria1*$^{fl/fl}$::*Gria2*$^{fl/fl}$::*Gria3*$^{fl/fl}$::*Grin1*$^{fl/fl}$), both the density and the percentage of activated rNSCs were not significantly different from each other (Figures S5F and S5G). In addition, the rNSC pool did not change significantly in quintuple transgenic mice compared to the controls (Figure S5H). These results suggest that glutamate signaling does not exert a significant effect on rNSC quiescence at the baseline condition, thus providing the functional support that inhibition of MC activity leads to increased activation of rNSCs through a reduction in the functionally dominant GABAergic indirect pathway.

Chronic Ablation of MCs Leads to a Transient Increase of rNSC Activation Followed by rNSC Pool Depletion

Our data showed that MC activity bi-directionally regulated rNSC quiescence. However, long-term consequences of altered

Figure 7. Chronic Ablation of MCs Leads to a Transient Increase of rNSC Activation Followed by rNSC Pool Depletion

(A) Viral injection scheme and experimental paradigm for chronic ablation of MCs using caspase system in 5htr2A-Cre mice.

(B) AAV-DIO-mCherry-labeled MCs and their commissural projections in mCherry only or mCherry and caspase co-injected animals at 21 dpi. Scale bars, 20 μm.

(C) Hilar GluR2/3$^+$ MCs in animals injected with AAV-flex-taCaspase3 versus AAV-DIO-eYFP at 21 dpi. Scale bar, 50 μm.

(D) Density of GluR2/3$^+$ MCs remaining in injected hilus at 15 and 21 dpi (n = 3, 4 in control, n = 5, 4 in caspase, at 15, 21 dpi).

(E) GABA$^+$ interneurons in the hilus injected with AAV-flex-taCaspase3 versus AAV-DIO-eYFP at 21 dpi. Scale bar, 50 μm.

(F) Density of GABA$^+$ interneurons remaining in the injected hilus at 21 dpi (n = 4).

(G, I, and K) Activated rNSCs (G), percentage of activated rNSCs (I), and rNSC pool (K) at various time points after MC ablation (n = 4, 3, 4, 3 in control; n = 4, 5, 4, 4 in caspase, at 10, 15, 21, 42 dpi).

(H, J, and L) Time course of normalized fold change in density and percentage of activated rNSCs (H and J) and rNSC pool (L) (n = 4, 3, 4, 3 mice in control group; n = 4, 5, 4, 4 mice in caspase group, at 10, 15, 21, 42 dpi).

Values represent mean ± SEM. Significance was determined based on $p < 0.05$ (n.s: $p > 0.05$; *$p < 0.05$; **$p < 0.01$; ***$p < 0.001$). See also Figure S6.

rNSC quiescence resulting from disrupted MC activity remain unknown. This may be particularly relevant, since many neuropathological states are associated with disrupted adult neurogenesis. To chronically manipulate MCs, we selectively ablated MCs and their projections by unilaterally injecting Cre-dependent AAV expressing the pro-apoptotic protease caspase 3 (AAV-FLEX-taCasp3-TEVp) to one hilus of adult 5htr2A-Cre mice (Yang et al., 2013) (Figure 7A). We examined ablation of MC somas and commissural projections by injecting a mixture of AAV-DIO-mCherry and AAV-Flex-taCasp3-2A-TEVp and observed no mCherry labeling at both injection and contralateral sides 21 days post AAV injection, compared to sham controls (Figure 7B), suggesting that the caspase virus is efficient in ablating MCs. Furthermore, we quantified the percentage of GluR2/3$^+$ MCs in caspase mice as compared to control mice at 15 and 21 days post viral injection and found 10% and 55% reduction of GluR2/3$^+$ MCs in caspase mice at 15 and 21 days post injection (dpi), respectively (Figures 7C and 7D). The result at 21 dpi is unexpected but intriguing, as the 5htr2A-Cre line only labels 24% of total MC population but caused 55% reduction of the MC population upon ablation, thus suggesting that targeting a small number of MCs could induce the death of a large number of them. Additionally, we quantified the density of GABA$^+$ cells in caspase mice at 21 dpi as compared to the control mice and found no significant difference between control and caspase groups (Figures 7E and 7F), suggesting that caspase ablation was specific to MCs.

Using this system, we then examined rNSC activation and maintenance at the commissural projection side following ablation of MCs at 10, 15, 21, and 42 days (Figure 7A). Interestingly, we observed a transient increase in the density and percentage of activated rNSCs at 15 dpi (Figures 7G–7J), suggesting that MC ablation acted upon the initial stages of adult rNSC lineage, which starts with symmetric self-renewing divisions of rNSCs followed by a self-depleting division (Götz, 2018; Pilz et al., 2018). We furthermore observed an increased rNSC pool (not statistically significant) along with increased rNSC proliferation at 15 dpi (Figures 7K and 7L). Importantly, our time course analysis (10, 15, 21, and 42 dpi) revealed that the transient increase of rNSC activation at 15 dpi was followed by rNSC pool depletion at 21 and 42 dpi (Figures 7H, 7J, and 7L), suggesting that increased rNSC proliferation leads to precocious depletion of the rNSC pool.

In the adult mouse DG, lineage tracing has shown that activated Nestin$^+$ rNSCs give rise to highly proliferative Tbr2$^+$ intermediate progenitors, which in turn generate mitotic DCX$^+$ neuroblasts. We examined the density of proliferating populations, including EdU$^+$, EdU$^+$Tbr2$^+$ intermediate progenitor cells, and EdU$^+$DCX$^+$ neuroblasts at various time points after MC ablation (Figures S6A–S6C). Interestingly, the density of mitotic neuroblasts (EdU$^+$DCX$^+$) (Figure S6A), but not intermediate progenitors (EdU$^+$Tbr2$^+$) (Figure S6B) and overall proliferating population (EdU$^+$) (Figure S6C), was significantly reduced in the caspase group at 42 dpi, but not 21 dpi, without affecting the density of overall DCX$^+$ population during this time frame (Figure S6D), suggesting that chronic MC ablation led to impaired production of mitotic neuroblasts, likely resulting from a decreased rNSC pool.

DISCUSSION

MCs are a major population of excitatory neurons in the adult hippocampus and are critically important in circuit functions of this region. Recent *in vivo* electrophysiology and intrinsic calcium imaging studies convincingly link unique MC circuits and properties to pattern separation (Danielson et al., 2017; GoodSmith et al., 2017; Senzai and Buzsáki, 2017). However, how MCs might contribute to the regulation of adult NSCs and hippocampal neurogenesis remains unknown. In this study, we identified MCs as a critical stem cell niche component that regulates rNSC quiescence and pool maintenance though the balance of indirect GABAergic\direct glutamatergic pathways under various activity states (Figure S7). Strikingly, a small subset of MCs containing the 5ht2A receptor is necessary for maintaining rNSC quiescence, since genetic ablation of this small population significantly reduced the rNSC pool and impaired hippocampal neurogenesis. Our findings have a number of implications for understanding basic mechanisms underlying dynamic control of adult hippocampal neurogenesis and for developing strategies to treat neurological disorders arising from aberrant adult hippocampal neurogenesis.

Our study showed that MCs provide both direct excitatory glutamatergic signaling onto rNSCs and indirect GABAergic signaling onto rNSCs mediated in part by dentate PV interneurons. Moreover, our morphological data suggest that the direct pathway is mediated by the commissural projection in the IML, while the indirect pathway is mediated by projections terminating on local interneurons in the SGZ or the hilus. Supporting this notion, recent ultrastructural analysis demonstrated that the bushy processes of rNSCs wrap around glutamatergic synapses likely formed between MCs and mature GCs (Moss et al., 2016). Additionally, comparative recordings of patches from soma versus radial processes demonstrated that glutamatergic receptors are present in the radial processes, but not the soma, of the rNSCs (Renzel et al., 2013). Functionally, we identified a critical role of MC activity states in regulating rNSC quiescence. Specifically, when MCs were activated at a moderate level, the indirect pathway played a dominant role by maintaining hyperpolarized rNSCs in order to prevent activation. In contrast, when MCs were inhibited, inhibition of the indirect pathway appeared to play a dominant role by allowing depolarization of the rNSCs, which increased activation of rNSCs. Together, these results suggest that the MC indirect pathway, but not the direct pathway, dictates rNSC quiescence by regulating the membrane potential of the rNSCs when MCs are either activated at a moderate level or inhibited. It is worth mentioning that the activation state of MCs is a relative definition that only correlates with the CNO dose used for these experiments. Both *in vitro* electrophysiology and *in vivo* calcium imaging analysis has demonstrated that MCs are more active than dentate GCs (Danielson et al., 2017; Scharfman, 1995). The active basal state of MCs was also confirmed by our calcium imaging analysis of 5htr2A-expressing MCs in acute brain slices showing that MCs typically exhibit a high level of spontaneous activity. However, when MCs are activated at the high level, the balance of indirect and direct pathways onto rNSCs is shifted from ''indirect pathway dominant'' to ''direct pathway dominant.'' This high activation

state may represent a pathological condition called "irritable MCs," which has been associated with network hyperexcitability and seizures (Scharfman and Myers, 2013) and could in turn induce rNSC activation and subsequent differentiation into reactive astrocytes (Sierra et al., 2015). In contrast to the dynamic regulation of rNSCs by MC activation, we found that chemogenetic inhibition and chronic ablation of MCs led to a transient increase of rNSC activation. However, rNSC depletion only occurs upon chronic ablation of MCs. These results suggest that chemogenetic inhibition of MCs and genetic ablation of MCs represent distinct conditions that induce disparate activity patterns onto rNSCs. Killing the MCs has quite a different effect than simply inhibiting their functional activity and may reflect consequences arising from the loss of spontaneous synaptic vesicle release at MC terminals. It is also likely that long-term inhibition of MCs may induce circuit adaptation or DREADD receptor desensitization. Taken together, our results suggest that fine-tuned MC activity is critical for maintaining rNSC quiescence and preserving the rNSC pool.

Interestingly, regulation of rNSCs under various MC activity states appears to be similar to how mature GCs are regulated. Recent studies showed that optogenetic activation of MC contralateral projections exerted a net inhibitory effect on GCs through disynaptic inhibition by preferentially recruiting basket cells (Hsu et al., 2016). Furthermore, MC loss caused a disinhibition and transient hyperexcitability of GCs (Jinde et al., 2012). Recent modeling data also concluded that deletion of the direct excitatory pathway would have little effect on GC excitability, but deletion of the indirect inhibitory pathways by deleting MC-basket cell connection would significantly increase GC excitability (Danielson et al., 2017). Together, these results indicate that rNSC activity is a reflection of the dentate network activity. This fits our previous model that rNSCs do not have synapses and therefore sense the dentate network activity through tonic GABA signaling mediated by spillover from synapses formed between PV cells and mature GCs (Moss and Toni, 2013; Song et al., 2012). Additionally, our data provide a plausible explanation for the dominant role of the MC indirect pathway in maintaining an inhibitory tone for both rNSCs and mature GCs to prevent over-activation. Excessive activation of rNSCs may lead to rNSC pool depletion and hyperexcitability of the hippocampal network (Sierra et al., 2015), and our results suggest that both aspects can be induced by reduced MC activity or the loss of MCs.

Chemogenetic activation of MCs promoted quiescence of contralateral rNSCs in both WT (moderate MC activation) and 5htr2A-Cre (high MC activation) mice. This raised the question of whether ipsilateral rNSCs are similarly regulated by MCs. We examined rNSC quiescence at the ipsilateral DG (i.e., injection side) in both WT and 5htr2A-Cre mice and did not observe significant alteration of rNSC quiescence in either mouse line (data not shown). However, these results are not conclusive, because non-specific labeling of granule cells in WT mice and CA3c pyramidal cells in 5htr2A-Cre mice would likely increase the activation of rNSCs, counteracting the inhibitory effects of MCs on rNSC quiescence. Future efforts in developing mouse lines that can exclusively target MCs will be able to provide definitive answers to this question.

Our study using 5htr2A-Cre mice showed that a small subset of MCs constituting approximately a quarter of the total MC population are both necessary and sufficient in regulating rNSC quiescence. Genetic ablation of this small population of MCs results in a transient increase of rNSC activation followed by significant reduction of the rNSC pool and impaired hippocampal neurogenesis. These results demonstrate how a small subset of MCs exert powerful effects on rNSC behaviors and hippocampal neurogenesis. Whether this small population of MCs represents a molecularly and functionally distinct subset of MCs remains unknown. Future investigations using single-cell sequencing in combination with circuit-based approaches to selectively label specific MC subpopulations could further address this question. MCs are particularly vulnerable to ischemia, traumatic brain injury, and seizures. Our study suggests that MC loss in these conditions, even in a small number, could potentially lead to aberrant hippocampal neurogenesis and associated cognitive deficits. Furthermore, a recent study demonstrated that activation of remaining MCs after chronic temporal lobe epilepsy alleviates seizure severity, while inhibition of those MCs impairs cognitive functions (Bui et al., 2018). Therefore, targeting the MC circuit by enhancing the indirect pathway or dampening the direct pathway may constitute a therapeutic strategy to combat hippocampal hyperexcitability associated with various neurological disorders and brain injuries in order to preserve neural stem cell pool, maintain sustainable hippocampal neurogenesis, and promote cognitive functions.

STAR★METHODS

Detailed methods are provided in the online version of this paper and include the following:

- KEY RESOURCES TABLE
- CONTACT FOR REAGENT AND RESOURCE SHARING
- EXPERIMENTAL MODEL AND SUBJECT DETAILS
- METHOD DETAILS
  - Tamoxifen Administration
  - Stereotaxic Surgery
  - Tissue Process and Immunohistochemistry
  - Imaging
  - Slice Electrophysiology
  - $Ca2^{+}$ Imaging
  - Electron Microscopy
- QUANTIFICATION AND STATISTICAL ANALYSIS
  - General
  - Cell Quantification
  - Slice Electrophysiology
  - Ca^{2+} Imaging
- DATA AND SOFTWARE AVAILABILITY

SUPPLEMENTAL INFORMATION

Supplemental Information includes seven figures and four videos and can be found with this article online at https://doi.org/10.1016/j.neuron.2018.07.010.

ACKNOWLEDGMENTS

We thank members of the Song lab for comments and discussions. This work was supported by grants awarded to J.S. from NARSAD (Brain and Behavior

Research Foundation), American Heart Association (14SDG20440029), Whitehall Foundation, and NIH (MH111773, MH106939, and AG058160). B.A. was partially supported by a NARSAD Young Investigator Award. N.T., J.M., F.C., and E.G. were supported by funds from the Swiss National Science Foundation (Nb. 31003A_173128) and Synapsis Foundation. We also thank the NIH-funded UNC Neuroscience Microscopy Core (P30 NS045892 and U54 HD079124) for its support of this work.

AUTHOR CONTRIBUTIONS

J.S. conceived the project, designed the experiments, and wrote the manuscript. N.T. led EM and enriched environment experiments. C.-Y.Y. performed *in vivo* functional analysis and surgeries for all the experiments. B.A. performed the electrophysiology and calcium imaging analysis. C.-Y.Y., B.A., and N.T. wrote part of the manuscript. J.M. and N.T. performed EM. L.J.Q., T.H., and H.B. assisted experiments and analysis. F.C. and E.G. performed enriched environment experiments. X.M and W.L provided quintuple transgenic mice and assisted related experiments.

DECLARATION OF INTERESTS

The authors declare no competing interests.

Received: October 1, 2017
Revised: May 16, 2018
Accepted: July 5, 2018
Published: July 26, 2018

REFERENCES

Adesnik, H., Li, G., During, M.J., Pleasure, S.J., and Nicoll, R.A. (2008). NMDA receptors inhibit synapse unsilencing during brain development. Proc. Natl. Acad. Sci. USA *105*, 5597–5602.

Buckmaster, P.S., Wenzel, H.J., Kunkel, D.D., and Schwartzkroin, P.A. (1996). Axon arbors and synaptic connections of hippocampal mossy cells in the rat in vivo. J. Comp. Neurol. *366*, 271–292.

Bui, A.D., Nguyen, T.M., Limouse, C., Kim, H.K., Szabo, G.G., Felong, S., Maroso, M., and Soltesz, I. (2018). Dentate gyrus mossy cells control spontaneous convulsive seizures and spatial memory. Science *359*, 787–790.

Chancey, J.H., Poulsen, D.J., Wadiche, J.I., and Overstreet-Wadiche, L. (2014). Hilar mossy cells provide the first glutamatergic synapses to adult-born dentate granule cells. J. Neurosci. *34*, 2349–2354.

Danielson, N.B., Turi, G.F., Ladow, M., Chavlis, S., Petrantonakis, P.C., Poirazi, P., and Losonczy, A. (2017). In vivo imaging of dentate gyrus mossy cells in behaving mice. Neuron *93*, 552–559.e4.

Deshpande, A., Bergami, M., Ghanem, A., Conzelmann, K.K., Lepier, A., Götz, M., and Berninger, B. (2013). Retrograde monosynaptic tracing reveals the temporal evolution of inputs onto new neurons in the adult dentate gyrus and olfactory bulb. Proc. Natl. Acad. Sci. USA *110*, E1152–E1161.

Gangarossa, G., Longueville, S., De Bundel, D., Perroy, J., Hervé, D., Girault, J.A., and Valjent, E. (2012). Characterization of dopamine D1 and D2 receptor-expressing neurons in the mouse hippocampus. Hippocampus *22*, 2199–2207.

Gebara, E., Bonaguidi, M.A., Beckervordersandforth, R., Sultan, S., Udry, F., Gijs, P.J., Lie, D.C., Ming, G.L., Song, H., and Toni, N. (2016). Heterogeneity of radial glia-like cells in the adult hippocampus. Stem Cells *34*, 997–1010.

GoodSmith, D., Chen, X., Wang, C., Kim, S.H., Song, H., Burgalossi, A., Christian, K.M., and Knierim, J.J. (2017). Spatial representations of granule cells and mossy cells of the dentate gyrus. Neuron *93*, 677–690.e5.

Götz, M. (2018). Revising concepts about adult stem cells. Science *359*, 639–640.

Grubb, M.S., and Burrone, J. (2010). Channelrhodopsin-2 localised to the axon initial segment. PLoS ONE *5*, e13761.

Gu, X., Zhou, L., and Lu, W. (2016). An NMDA receptor-dependent mechanism underlies inhibitory synapse development. Cell Rep. *14*, 471–478.

Hsu, T.T., Lee, C.T., Tai, M.H., and Lien, C.C. (2016). Differential recruitment of dentate gyrus interneuron types by commissural versus perforant pathways. Cereb. Cortex *26*, 2715–2727.

Hutchison, M.A., Gu, X., Adrover, M.F., Lee, M.R., Hnasko, T.S., Alvarez, V.A., and Lu, W. (2018). Genetic inhibition of neurotransmission reveals role of glutamatergic input to dopamine neurons in high-effort behavior. Mol. Psychiatry *23*, 1213–1225.

Jia, H., Rochefort, N.L., Chen, X., and Konnerth, A. (2011). In vivo two-photon imaging of sensory-evoked dendritic calcium signals in cortical neurons. Nat. Protoc. *6*, 28–35.

Jinde, S., Zsiros, V., Jiang, Z., Nakao, K., Pickel, J., Kohno, K., Belforte, J.E., and Nakazawa, K. (2012). Hilar mossy cell degeneration causes transient dentate granule cell hyperexcitability and impaired pattern separation. Neuron *76*, 1189–1200.

Kuo, C.T., Mirzadeh, Z., Soriano-Navarro, M., Rasin, M., Wang, D., Shen, J., Sestan, N., Garcia-Verdugo, J., Alvarez-Buylla, A., Jan, L.Y., and Jan, Y.N. (2006). Postnatal deletion of Numb/Numblike reveals repair and remodeling capacity in the subventricular neurogenic niche. Cell *127*, 1253–1264.

Lu, W., Shi, Y., Jackson, A.C., Bjorgan, K., During, M.J., Sprengel, R., Seeburg, P.H., and Nicoll, R.A. (2009). Subunit composition of synaptic AMPA receptors revealed by a single-cell genetic approach. Neuron *62*, 254–268.

Lu, W., Bushong, E.A., Shih, T.P., Ellisman, M.H., and Nicoll, R.A. (2013). The cell-autonomous role of excitatory synaptic transmission in the regulation of neuronal structure and function. Neuron *78*, 433–439.

Mignone, J.L., Kukekov, V., Chiang, A.S., Steindler, D., and Enikolopov, G. (2004). Neural stem and progenitor cells in nestin-GFP transgenic mice. J. Comp. Neurol. *469*, 311–324.

Moss, J., and Toni, N. (2013). A circuit-based gatekeeper for adult neural stem cell proliferation: parvalbumin-expressing interneurons of the dentate gyrus control the activation and proliferation of quiescent adult neural stem cells. BioEssays *35*, 28–33.

Moss, J., Gebara, E., Bushong, E.A., Sánchez-Pascual, I., O'Laoi, R., El M'Ghari, I., Kocher-Braissant, J., Ellisman, M.H., and Toni, N. (2016). Fine processes of Nestin-GFP-positive radial glia-like stem cells in the adult dentate gyrus ensheathe local synapses and vasculature. Proc. Natl. Acad. Sci. USA *113*, E2536–E2545.

Otis, J.M., Namboodiri, V.M., Matan, A.M., Voets, E.S., Mohorn, E.P., Kosyk, O., McHenry, J.A., Robinson, J.E., Resendez, S.L., Rossi, M.A., and Stuber, G.D. (2017). Prefrontal cortex output circuits guide reward seeking through divergent cue encoding. Nature *543*, 103–107.

Pilz, G.A., Bottes, S., Betizeau, M., Jörg, D.J., Carta, S., Simons, B.D., Helmchen, F., and Jessberger, S. (2018). Live imaging of neurogenesis in the adult mouse hippocampus. Science *359*, 658–662.

Puighermanal, E., Biever, A., Espallergues, J., Gangarossa, G., De Bundel, D., and Valjent, E. (2015). drd2-cre:ribotag mouse line unravels the possible diversity of dopamine d2 receptor-expressing cells of the dorsal mouse hippocampus. Hippocampus *25*, 858–875.

Renzel, R., Sadek, A.R., Chang, C.H., Gray, W.P., Seifert, G., and Steinhäuser, C. (2013). Polarized distribution of AMPA, but not GABAA, receptors in radial glia-like cells of the adult dentate gyrus. Glia *61*, 1146–1154.

Ribak, C.E., and Seress, L. (1983). Five types of basket cell in the hippocampal dentate gyrus: a combined Golgi and electron microscopic study. J. Neurocytol. *12*, 577–597.

Rothman, J.S., and Silver, R.A. (2018). NeuroMatic: an integrated open-source software toolkit for acquisition, analysis and simulation of electrophysiological data. Front. Neuroinform. *12*, 14.

Scharfman, H.E. (1995). Electrophysiological evidence that dentate hilar mossy cells are excitatory and innervate both granule cells and interneurons. J. Neurophysiol. *74*, 179–194.

Scharfman, H.E. (2016). The enigmatic mossy cell of the dentate gyrus. Nat. Rev. Neurosci. *17*, 562–575.

Scharfman, H.E., and Myers, C.E. (2013). Hilar mossy cells of the dentate gyrus: a historical perspective. Front. Neural Circuits *6*, 106.

Senzai, Y., and Buzsáki, G. (2017). Physiological properties and behavioral correlates of hippocampal granule cells and mossy cells. Neuron *93*, 691–704.e5.

Shin, J., Berg, D.A., Zhu, Y., Shin, J.Y., Song, J., Bonaguidi, M.A., Enikolopov, G., Nauen, D.W., Christian, K.M., Ming, G.L., and Song, H. (2015). Single-cell RNA-seq with waterfall reveals molecular cascades underlying adult neurogenesis. Cell Stem Cell *17*, 360–372.

Sierra, A., Martín-Suárez, S., Valcárcel-Martín, R., Pascual-Brazo, J., Aelvoet, S.A., Abiega, O., Deudero, J.J., Brewster, A.L., Bernales, I., Anderson, A.E., et al. (2015). Neuronal hyperactivity accelerates depletion of neural stem cells and impairs hippocampal neurogenesis. Cell Stem Cell *16*, 488–503.

Song, J., Zhong, C., Bonaguidi, M.A., Sun, G.J., Hsu, D., Gu, Y., Meletis, K., Huang, Z.J., Ge, S., Enikolopov, G., et al. (2012). Neuronal circuitry mechanism regulating adult quiescent neural stem-cell fate decision. Nature *489*, 150–154.

Song, J., Sun, J., Moss, J., Wen, Z., Sun, G.J., Hsu, D., Zhong, C., Davoudi, H., Christian, K.M., Toni, N., et al. (2013). Parvalbumin interneurons mediate neuronal circuitry-neurogenesis coupling in the adult hippocampus. Nat. Neurosci. *16*, 1728–1730.

Song, J., Olsen, R.H., Sun, J., Ming, G.L., and Song, H. (2016). Neuronal circuitry mechanisms regulating adult mammalian neurogenesis. Cold Spring Harb. Perspect. Biol. *8*, 8.

Sternson, S.M., and Roth, B.L. (2014). Chemogenetic tools to interrogate brain functions. Annu. Rev. Neurosci. *37*, 387–407.

Tanaka, K.F., Samuels, B.A., and Hen, R. (2012). Serotonin receptor expression along the dorsal-ventral axis of mouse hippocampus. Philos. Trans. R. Soc. Lond. B Biol. Sci. *367*, 2395–2401.

Ting, J.T., Daigle, T.L., Chen, Q., and Feng, G. (2014). Acute brain slice methods for adult and aging animals: application of targeted patch clamp analysis and optogenetics. Methods Mol. Biol. *1183*, 221–242.

Vivar, C., Potter, M.C., Choi, J., Lee, J.Y., Stringer, T.P., Callaway, E.M., Gage, F.H., Suh, H., and van Praag, H. (2012). Monosynaptic inputs to new neurons in the dentate gyrus. Nat. Commun. *3*, 1107.

Yang, C.F., Chiang, M.C., Gray, D.C., Prabhakaran, M., Alvarado, M., Juntti, S.A., Unger, E.K., Wells, J.A., and Shah, N.M. (2013). Sexually dimorphic neurons in the ventromedial hypothalamus govern mating in both sexes and aggression in males. Cell *153*, 896–909.

STAR★METHODS

KEY RESOURCES TABLE

REAGENT or RESOURCE	SOURCE	IDENTIFIER
Antibodies		
Anti-Rabbit GluR2/3	Millipore	Cat# AB1506; RRID: AB_90710
Anti-Rabbit GABA	Sigma-Aldrich	Cat# A2052; RRID: AB_477652
Anti-Chicken Nestin	Aves	Cat# NES; RRID: AB_2314882
Anti-Rabbit GFAP	DAKO	Cat# Z0334; RRID: AB_10013382
Anti-Mouse Tbr2	Thermo Fisher Scientific	Cat# 14-4875-82; RRID: AB_11042577
Anti-Goat DCX	Santa Cruz	Cat# SC_8066; RRID: AB_2088494
Anti-Rabbit Ki67	Thermo Fisher Scientific	Cat# PA5-19462; RRID: AB_10981523
Anti-Mouse Parvalbumin	Swant	Cat# PV235; RRID: AB_10000343
Anti-Rabbit c-Fos	Santa Cruz	Cat# sc-52; RRID: AB_2106783
Anti-Goat GFP	Vector Laboratories	Cat# BA-0702; RRID: AB_2336121
Anti-Chicken GFP	Aves	Cat# GFP-1020; RRID: AB_10000240
Anti-Rat mCherry	Thermo Fisher Scientific	Cat# M11217; RRID: AB_2536611
Anti-Rabbit NR1	Abcam	Cat# 17345; RRID: AB_776808
Nanogold-anti-Rabbit	Nanoprobes	Cat# 2004; RRID: AB_2631182
Bacterial and Virus Strains		
AAV8-CaMKII-hM3Dq-mCherry	UNC Vector Core	No longer produced at UNC. Now available at Addgene #50476.
AAV8-CaMKII-eGFP	UNC Vector Core	N/A
AAV5-CaMKII-mCherry	UNC Vector Core	N/A
AAV8-CaMKII-HA-hM3Dq-mCitrine	UNC Vector Core	No longer produced at UNC. Provided by the Bryan Roth lab.
AAV5-CaMKII-hM4Di-mCherry	UNC Vector Core	No longer produced at UNC. Now available at Addgene #50477.
AAV5-CaMKII-ChR2-mCherry	UNC Vector Core	N/A
AAV2-hsyn-DIO-hM3Dq-mCherry	UNC Vector Core	No longer produced at UNC. Now available at Addgene #44361.
AAV2-Ef1α-DIO-mCherry	UNC Vector Core	N/A
AAV5-hsyn-DIO-mCherry	UNC Vector Core	No longer produced at UNC. Now available at Addgene #50459.
AAV5-hsyn-DIO-hM4Di-mCherry	UNC Vector Core	No longer produced at UNC. Now available at Addgene #44362.
AAV5-EF1α-DIO-eYFP	UNC Vector Core	N/A
AAV5-FLEX-taCasp3-TEVp	UNC Vector Core	N/A
AAVdj-CaMKII-GCaMP6s	Otis et al., 2017	Provided by the Garret Stuber lab
AAVdj-EF1α-DIO-GCaMP6s	Otis et al., 2017	Provided by the Garret Stuber lab
AAVdj-EF1α-DIO-GCaMP6f	Otis et al., 2017	Provided by the Garret Stuber lab
Chemicals, Peptides, and Recombinant Proteins		
5-Ethynyl-2′-deoxyuridine	Carbosynth	Cat# NE08701
Alexa Fluor 488 Azide	Thermo Fisher Scientifc	Cat# A10266
Alexa Fluor 594 Azide	Thermo Fisher Scientifc	Cat# A10270
Clozapine-N-Oxide (CNO)	NIMH Chemical Synthesis and Drug Supply program	Cat# C-929
Tamoxifen	Sigma-Aldrich	Cat# T5648
HQ Silver kit	Nanoprobe	Cat# 2012

(*Continued on next page*)

Continued

REAGENT or RESOURCE	SOURCE	IDENTIFIER
Experimental Models: Organisms/Strains		
C57BL/6	The Jackson Laboratory	RRID: IMSR_JAX:000664
VGAT-Cre (B6. *Slc32a1*$^{tm2(cre)Lowl}$)	The Jackson Laboratory	RRID: IMSR_JAX:016962
5htr2A-Cre (B6.Tg(*Htr2a-Cre*)KM208Gsat)	GENSAT	RRID: MMRRC_036679-UCD
PV-Cre (B6.129P2-*Pvalb*$^{tm1(cre)Arbr}$)	The Jackson Laboratory	RRID: IMSR_JAX:008069
Nestin-GFP	Mignone et al., 2004	Provided by the Grigori Enikolopov lab
Nestin-CreER$^{T2+/-}$;*Gria1-3*$^{fl/fl}$;*Grin1*$^{fl/fl}$	Lu et al., 2013	Provided by the Lu Wei lab
Software and Algorithms		
Fiji	ImageJ	RRID: SCR_002285; http://fiji.sc
GraphPad Prism 7	GraphPad Software	RRID: SCR_002798; https://www.graphpad.com/
FV10-ASW 4.2 viewer	Olympus	https://www.olympus-lifescience.com/en/support/downloads/
pClamp 10	Molecular Devices	N/A
NeuroMatic package	Rothman and Silver, 2018	RRID: SCR_004186; http://www.neuromatic.thinkrandom.com/
Igor Pro	Wavemetrics	RRID: SCR_000325

CONTACT FOR REAGENT AND RESOURCE SHARING

Further information and requests for resources and reagents should be directed to and will be fulfilled by the Lead Contact, Juan Song, Ph.D. (juansong@email.unc.edu).

EXPERIMENTAL MODEL AND SUBJECT DETAILS

Young adult mice (6-8 weeks, males and females) were used and randomly assigned to experimental groups. C57BL/6, VGAT-Cre (B6. *Slc32a1*$^{tm2(cre)Lowl}$) and PV-Cre (B6.129P2-*Pvalb*$^{tm1(cre)Arbr}$) mice were obtained from the Jackson laboratory, and have been back-crossed with C57BL/6 for at least 6 generations. Nestin-GFP mice were obtained from Dr. Grigori Enikolopov at Stony Brook University. 5htr2A-cre (B6.Tg(*Htr2a-Cre*)KM208Gsat) mice were from GENSAT (036679-UCD). *Gria1-3*$^{fl/fl}$*Grin1*$^{fl/fl}$ (F4 control) were generated as previously described (Lu et al., 2013). *Nestin-creER*$^{T2+/-}$; *Gria1-3*$^{fl/fl}$; *Grin1*$^{fl/fl}$ (cKO) were generated by crossing *Gria1-3*$^{fl/fl}$*Grin1*$^{fl/fl}$ mice with *Nestin-creER*^{T2} mice. All mice were experimentally and drug naive before procedure and no immune deficiency nor health problems were observed. Animals were grouped house in a 12 hr light/dark cycle with access to food and water *ad libitum*. After the surgeries, animals were relocated to a satellite facility for recovery. For enriched environment, eight-week old C57BL/6J male mice were housed for 13 days in either a normal housing cage, or an enriched environment. Normal housing consisted of: 3 mice per cage, standard cage, unlimited access to water and food, bedding and 1 cardboard tunnel. Enriched environment consisted of: 2x larger cages, 5 mice per cage, unlimited access to food and water, numerous toys (ladder, box, tubes, houses), 2 cardboard tunnels, bedding, nest material and a running wheel. All procedures followed NIH Guide for the Care and Use of Laboratory Animals and were approved by Institutional Animal Care and Use Committee at the University of North Carolina at Chapel Hill (UNC).

METHOD DETAILS

Tamoxifen Administration

Tamoxifen (Sigma) was prepared in corn coil at a concentration of 20 mg/ml. F4 control and cKO mice were given Tamoxifen (100 mg/kg) via intraperitoneal injection (i.p.) daily for 7 consecutive days at the age of 8 weeks old. Animals were sacrificed for tissue collection 4 weeks after the last injection.

Stereotaxic Surgery

In brief, young adult mice (6-8 weeks) were anesthetized under 1%–2% isoflurane in oxygen at 0.6-0.8 LPM flow rate. AAV vectors were injected stereotaxically to the DG using the following coordinate: AP −2.0 mm, ML ± 1.5 mm, DV −2.3 mm from Bregma, with microsyringe (Hamilton, 33GA) and microinjection pump (Hamilton) at a speed of 100 nl/min. Mice were allowed to recover for 2-3 weeks from the surgery before *in vivo* or *ex vivo* experiments. For *in vivo* DREADD experiments, mice in C57BL/6 background were injected unilaterally with AAV8-CaMKII-hM3Dq-mCherry, AAV8-CaMKII-hM4Di-mCherry, AAV8-CaMKII-hM3Dq-mCerry, AAV5-CaMKII-mCherry or AAV8-CAMKII-eGFP into DG. 5htr2A-Cre mice were injected unilaterally with AAV2-hsyn-DIO-hM3Dq-mCherry, AAV5-hsyn-DIO-hM4Di-mCherry, AAV2-EF1α-DIO-mCherry or AAV5-hsyn-DIO-mCherry into the DG. Animals were given

2-week recovery and subject to CNO treatment by adding CNO to drinking water at a concentration of 0.25 mg/200 mL or 1 mg/200 mL for 4 or 21 days. CNO was provided by NIH as part of the Rapid Access to investigative Drug Program funded by NINDS. On the last day, mice were given i.p. injection of EdU (40 mg/kg, Carbosynth) for 4 times with a 2-hr interval. Mice were perfused 2 hr after the last EdU injection. For c-Fos experiments, injected mice were given i.p. injection of 0.25 mg/kg or 1 mg/kg CNO and perfused 90 min after i.p. injection. For Caspase3-mediated ablation, 5htr2A-cre mice were injected with AAV5-FLEX-taCasp3-TEVp or AAV5-EF1a-DIO-eYFP unilaterally into the DG, and perfused at 10, 15, 21 or 42 days post viral injection (dpi) for immunohistochemistry and analysis. For slice recording, viral injections were conducted in similar ways. Additional AAV vectors including AAV8-CaMKII-HA-hM3Dq-IRES-mCitrine, AAV5-CaMKII-ChR2-mCherry, AAV5-hysn-DIO-mCherry, AAVdj-CaMKII-GCaMP6s, AAVdj-EF1α-DIO-GCaMP6f, and AAVdj-EF1α-DIO-GCaMP6s were injected into the DG of adult mice for different experiments. Mice were used for slice preparation and electrophysiological recording 2-4 weeks after viral injection. No specific replication designs were used, but multiple animals were used as indicated in the figure legends. Sample size estimation was based on previous publications and power analysis. Mice with viral expression outside the region of interest (DG) were excluded from tissue processing and further analysis.

Tissue Process and Immunohistochemistry

Mice were anesthetized with isoflurane. Brains were fixed via aortic arch perfusion of ice-cold 4% paraformaldehyde (PFA) in phosphate buffered saline (PBS) at pH 7.4. Brains were collected and post-fixed in 4% PFA overnight, followed by 30% sucrose in PBS for 2-3 days. Brains were sectioned into 40 μm coronal sections with a microtome and stored in cryoprotectant solution containing 30% sucrose, 30% ethylene glycol in 0.1M phosphate buffer.

Tissues were rinsed with PBS and then 0.05% Triton X-100 in Tris-buffered saline (TBS^+), followed by 0.5% Triton X-100 in TBS (TBST) for 30 min and incubation in 3% donkey serum in TBS^+ for 30 min. The sections were then incubated in primary antibody overnight at 4°C. The sections were then rinsed with TBS^+ and incubated in secondary antibody at room temperature for 2 hr. All brain sections were mounted in an aqueous medium.

For Nestin immunostaining and detection of EdU, tissues were subjected to antigen retrieval treatment by incubating the sections in boiled 0.1M citrate buffer and microwaved to keep buffer boiling for 7 min as previously described (Song et al., 2012). Sections were permeabilized in TBST for 20-30 min and then incubated in click reaction buffer (0.1 M Tris, 0.5–1 mM $CuSO_4$, 30 μM 488/594 Alexa-azide, and 50–100 mM ascorbic acid) for 30 min for EdU labeling. Slides were then rinsed with TBS^+, followed by similar immunostaining steps as described above.

Imaging

Coronal sections through the entire hippocampus were collected in a serial order. Images were acquired by Olympus FLUOVIEW1000 or Zeiss LSM780 confocal microscope, under 40x Oil (NA 1.30), Z-resolution 1.0 or 1.5 μm/slice. Tiled images were acquired and stitched using Olympus FluoView or Zeiss Zen imaging software.

Slice Electrophysiology

Adult mice housed under standard conditions were used at 2-4 weeks post AAV injection for slice preparation. Animals were anesthetized under isoflurane and briefly perfused intra-cardially with 10 mL of ice-cold NMDG solution (Ting et al., 2014) containing (in mM): 92 NMDG, 30 $NaHCO_3$, 25 glucose, 20 HEPES, 10 $MgSO_4$, 5 sodium ascorbate, 3 sodium pyruvate, 2.5 KCl, 2 thiourea, 1.25 NaH_2PO_4, 0.5 $CaCl_2$ (pH 7.3, 300 mOsm, bubbled with 95% O_2 and 5% CO_2). The brains were then quickly removed into additional ice-cold NMDG solution for slicing. Transverse slices were cut using a Leica VT1200S vibratome at 280 μm thickness, and warmed to 36.5°C for 10 min. Slices were transferred to room temperature (22–24°C) HEPES holding solution (Ting et al., 2014) containing (in mM): 92 NaCl, 30 $NaHCO_3$, 25 glucose, 20 HEPES, 5 sodium ascorbate, 3 sodium pyruvate, 2.5 KCl, 2 thiourea, 2 $MgSO_4$, 2 $CaCl_2$, 1.25 NaH_2PO_4, (pH 7.3, 300 mOsm, bubbled with 95% O_2 and 5% CO_2) for 1 - 2 hr. Solutions intended for use with MC or PV recordings or for calcium imaging also contained 12 mM N-acetyl-L-cysteine in the NMDG and HEPES solutions to improve glutathione synthesis (Ting et al., 2014).

Electrophysiological recordings were obtained at 22–24°C in artificial CSF containing (in mM): 125 NaCl, 26 $NaHCO_3$, 20 glucose, 2.5 KCl, 2 $CaCl_2$, 1.3 $MgCl_2$, 1.25 NaH_2PO_4, (pH 7.3, 300 mOsm, bubbled with 95% O_2 and 5% CO_2) on a Scientifica SliceScope. GFP^+ neural stem cells within the sub-granule zone were visualized by DIC and fluorescence microscopy with a 40X water-dipping objective (LUMPlanFL N, 0.8; Olympus). Alternatively, subgranular YFP^+ PV neurons, or hilar $mCherry^+$ MCs were targeted for recordings. Microelectrodes (3–6 MΩ) were pulled from 1.5 mm diameter borosilicate glass capillaries (WPI) and filled with potassium based internal solution containing (in mM): 130 K-gluconate, 20 HEPES, 4 $MgCl_2$, 4 Na-ATP, 2 NaCl, 0.5 EGTA, 0.4 Na-GTP (pH 7.3, 310 mOsm). To stimulate ChR2 in mossy-cell terminals, single light-pulses (1 or 5 s) or trains of 5 ms light-pulses (at 1 or 10 Hz) were generated by a pE-100 (CoolLED) 470 nm LED and triggered via TTL control through the acquisition software, illuminating the tissue through the 40X objective. Pharmacological agents (Tocris) were used at the following final concentrations in the bath as indicated: bicuculline (50 μM), muscimol (100 μM), glutamate (100 μM), NBQX (10 μM), APV (100 μM), TTX (1 μM), and 4-AP (40 μM). Bath-applied CNO was used at concentrations of 0.25-50 μM, but typically 10 μM. All other chemicals were purchased from Sigma. Data were collected using a Multiclamp 700B amplifier and digitized with a DigiData 1440A (Axon Instruments) at 10 kHz using pClamp10 software. The whole-cell patch-clamp configuration was employed in current-clamp mode (with I = 0) to freely monitor membrane potential changes. Cell-attached recordings were made using filtered ACSF in the recording pipette, and collected in

voltage-clamp mode with no applied holding voltage (V = 0) and filtered at 6 kHz. Unstable whole-cell recordings (monitored by membrane test pulse) were excluded from analysis.

$Ca2^+$ Imaging

AAV-mediated DIO-GCaMP6f was selectively expressed in VGAT-Cre or PV-Cre mice, or with AAV-mediated DIO-GCaMP6s in 5htr2A-Cre mice. AAV-mediated GCaMP6s was expressed in C57BL/6 mice. Acute brain slices were prepared and observed as for electrophysiology. A CoolLED pE-100 at 470 nm was used for excitation, and GCaMP fluorescence was acquired through a standard GFP filter cube and captured with an Optimos sCMOS camera (Q-Imaging), using Micro Manager acquisition software. Image sequences were acquired at 100 to 500 ms frame rates with 6-7 focal-plane sections.

Electron Microscopy

6 adult male Nestin-GFP mice were used for immuno-electron microscopy. To examine contacts between rNSC and MC axons, mice were injected with AAV-CaMKII-eGFP. Mice were perfused with fixative (4% paraformaldehyde, w/v; 0.1% glutaraldehyde, v/v; in 0.1M phosphate buffer, PB; 10 min) and cut in 50 μm-thick coronal sections. Sections were cryoprotected, freeze-thawed 3 times and immunostained using the following antibodies: primary antibody (rabbit anti-NR1; Abcam, ab17345; 1:1000 or goat anti-GFP antibody, Vector Laboratories, BA0702; 1:1000) followed by the secondary antibody (goat anti-rabbit; 1:100; Nanoprobes, #2004; conjugated with 1.4 nm colloidal gold) followed by silver intensification (HQ Silver Kit; Nanoprobes) or avidin biotin peroxidase complex (ABC Elite; Vector Laboratories), followed by peroxidase reactions with 3, 3-diaminobenzidine (DAB; Vector Laboratories Kit).

All sections were washed in 0.1M PB, post-fixed with 1% osmium tetroxide in 0.1M PB and dehydrated in an ascending series of ethanol concentrations and acetone and then cured into resin. One hundred and twenty-four serial sections (70 nm thick) were cut, contrasted, and observed using a Philips CM10 transmission electron microscope. Low-magnification images (1,450×) were collected of each cell for each of the 124 sections and aligned for tracing and 3D reconstruction using Fiji ImageJ software. A sample of 10 sections, approximately 10 sections apart (700 nm) were selected for quantification of NR1 immunogold particles overlying peroxidase-labeled RGL stem cell processes. For these sections, processes of the RGL stem cell were captured at a higher magnification (5,800×) that allowed individual particles to be seen (approximately 5 images/section).

QUANTIFICATION AND STATISTICAL ANALYSIS

General

Mice from both genders were used for all experiments, as our previous studies have established that sex difference did not appear to contribute to observed statistical variation (Song et al., 2012, 2013). Mouse identity and experimental manipulation were coded, and the quantifications and analysis were performed blindly by a single observer. Two-tailed unpaired Student's t test was used to examine statistical difference by using Graphpad Prism 7 (Graphpad Software) or Igor Pro (Wavemetrics) if not otherwise specified. Paired Student's t tests were use where appropriate. Wilcoxon Rank test was used when sample variances were unequal as determined in Igor Pro statistics package. For all experimental results, "n" represents the number of animals used unless otherwise specified and is reported in figure legends. Data throughout are presented as mean ± SEM. Significance was determined based on $p < 0.05$ (n.s: $p > 0.05$, not significant; * $p < 0.05$; ** $p < 0.01$; *** $p < 0.001$).

Cell Quantification

Slide identities were blinded during quantification to avoid bias. For GluR2/3, GABA, c-Fos, Nestin-GFP, PV, Nestin/EdU, Tbr2/EdU, DCX/EDU, DCX, and EdU quantification, whole tilling DG images were acquired and quantified manually throughout z stacks.

Slice Electrophysiology

Electrophysiology traces were analyzed using a combination of the NeuroMatic package (by Jason Rothman, ThinkRandom.com) and custom built analysis routines, written for Igor Pro (Wavemetrics).

Ca^{2+} Imaging

Ca^{2+} fluorescent signals were analyzed using NIH ImageJ software and custom procedures written in Igor Pro (Wavemetrics). The change in calcium signal was determined from surround subtracted regions of interest and converted into ΔF/F values (Jia et al., 2011). Quantification of calcium event frequency was determined using peak detection algorithms and manual thresholding in Igor Pro.

DATA AND SOFTWARE AVAILABILITY

ImageJ is an open source software for image analysis. FV10-ASW 4.2 viewer is available on Olympus website. Neuromatic Package for Igor Pro is freely available from ThinkRandom.com. All others are commercial software. See Key Resources Table for details.

Neuron, Volume *99*

Supplemental Information

Mossy Cells Control Adult Neural Stem Cell Quiescence and Maintenance through a Dynamic Balance between Direct and Indirect Pathways

Chia-Yu Yeh, Brent Asrican, Jonathan Moss, Luis Jhoan Quintanilla, Ting He, Xia Mao, Frederic Cassé, Elias Gebara, Hechen Bao, Wei Lu, Nicolas Toni, and Juan Song

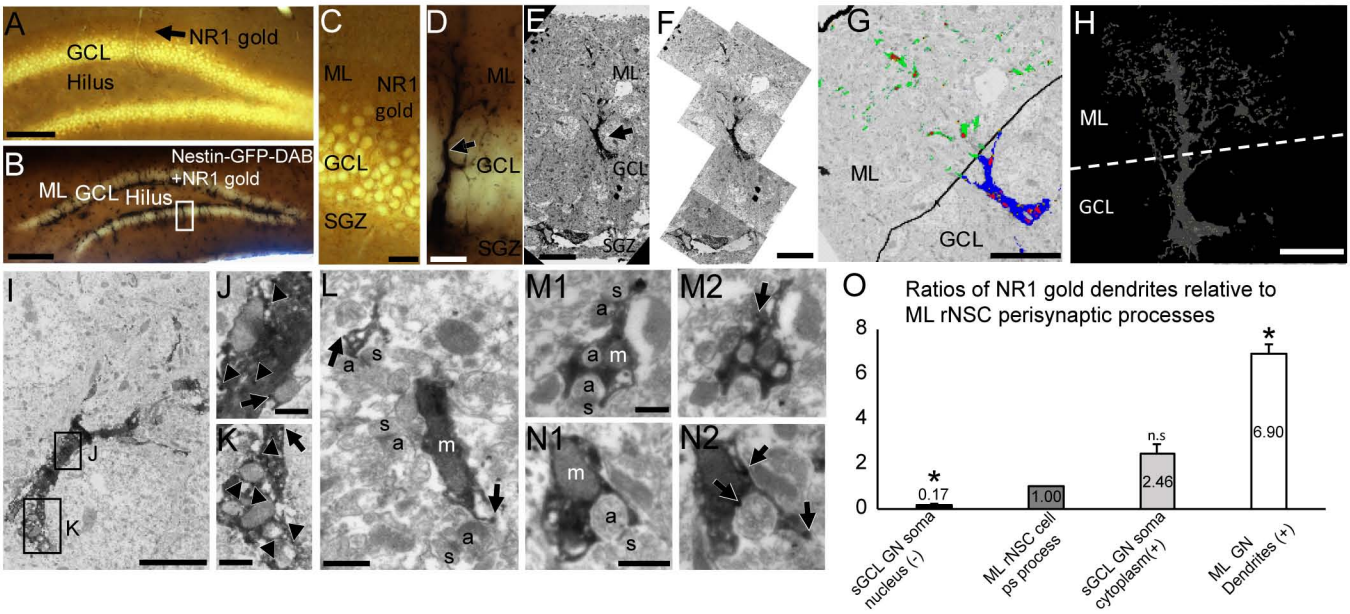

Figure S1. Yeh et al. 2018

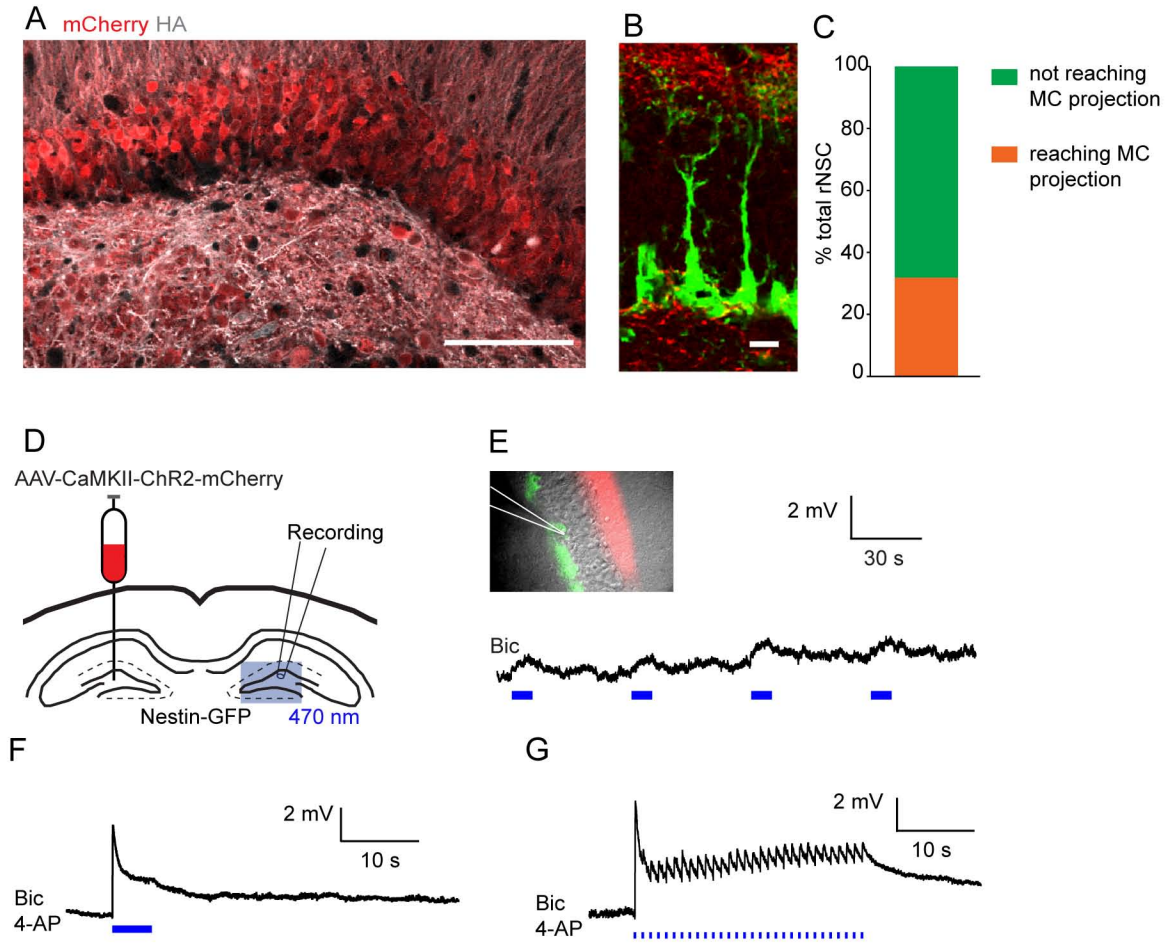

Figure S2. Yeh et al. 2018

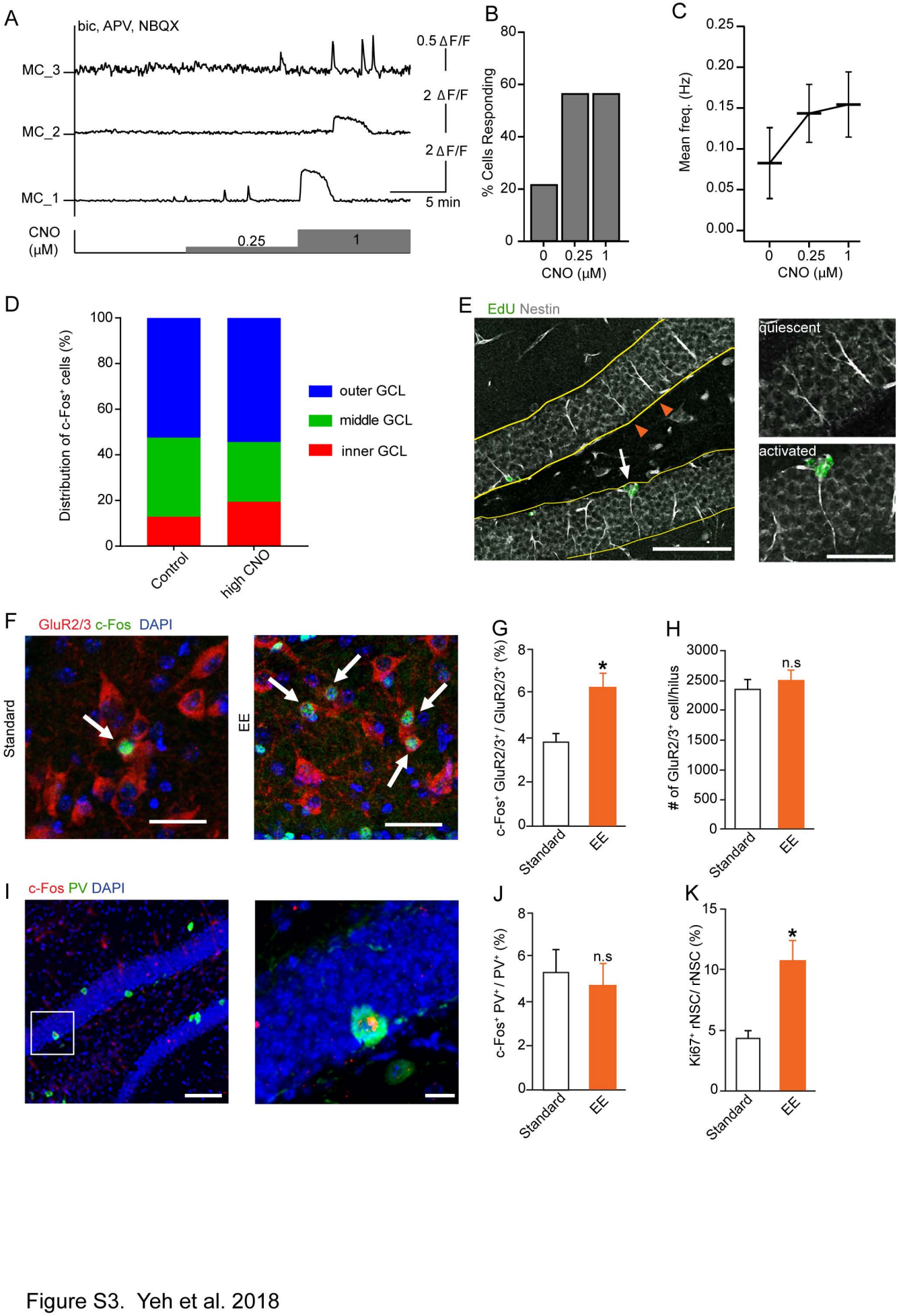

Figure S3. Yeh et al. 2018

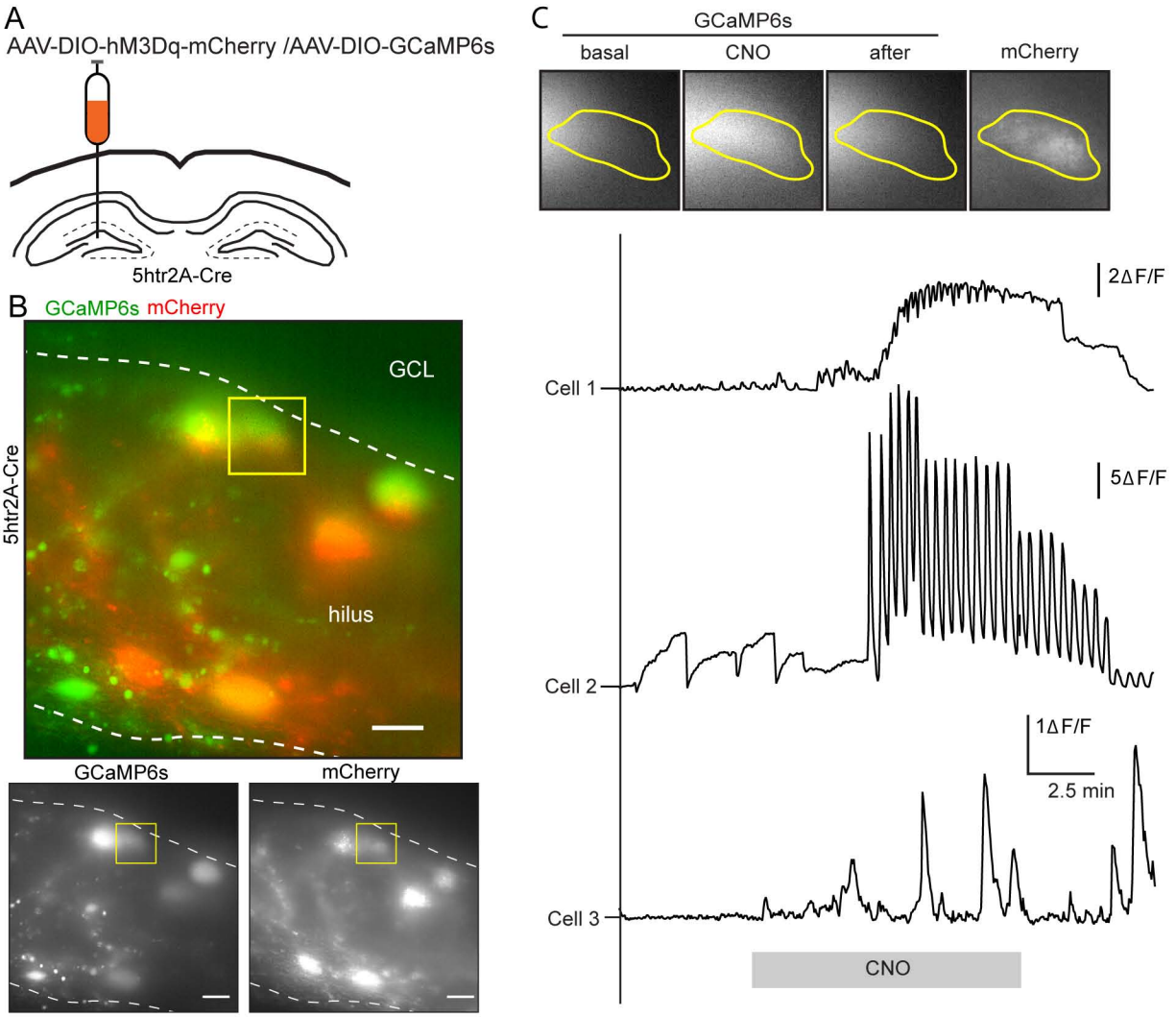

Figure S4. Yeh et al. 2018

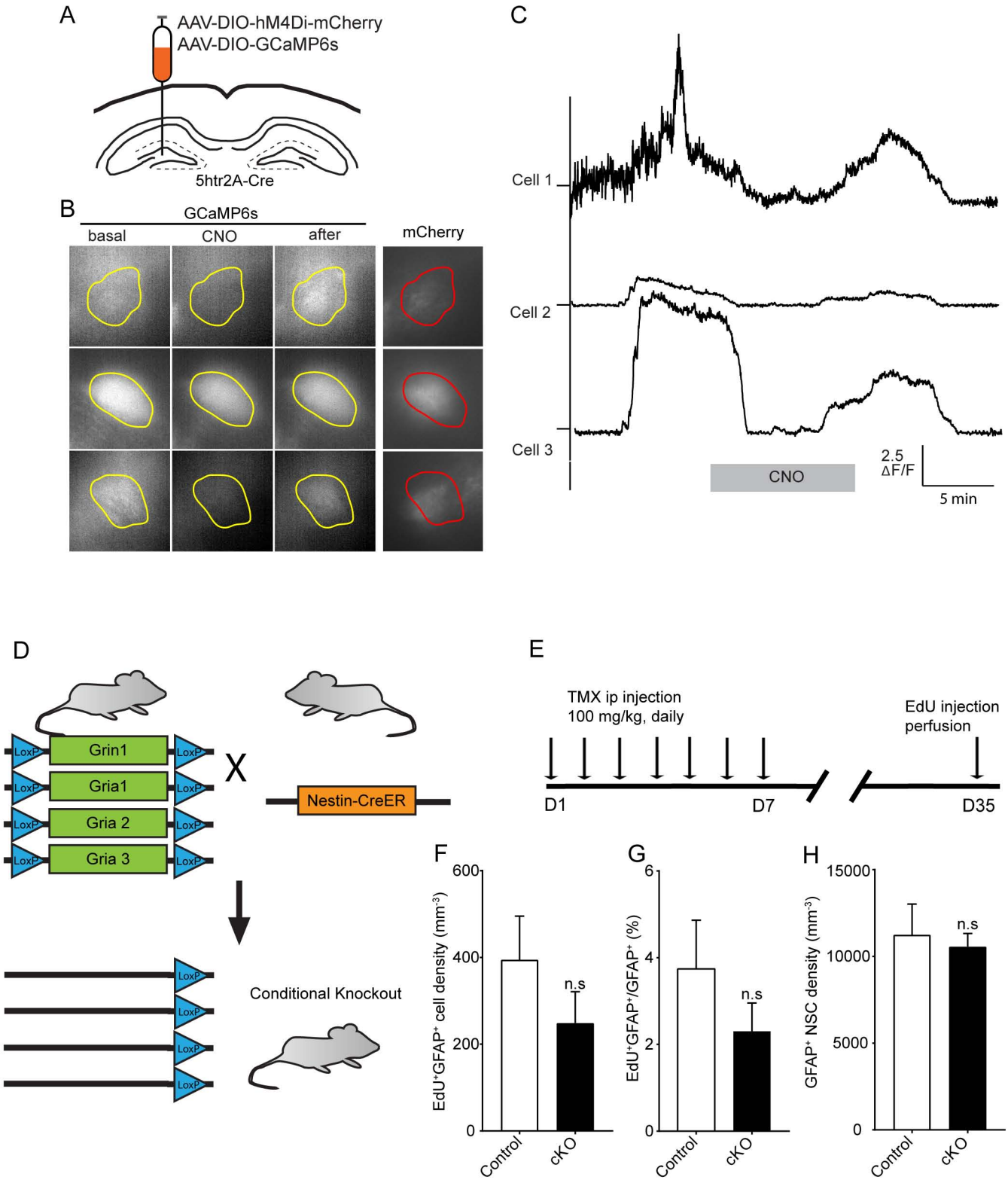

Figure S5. Yeh et al. 2018

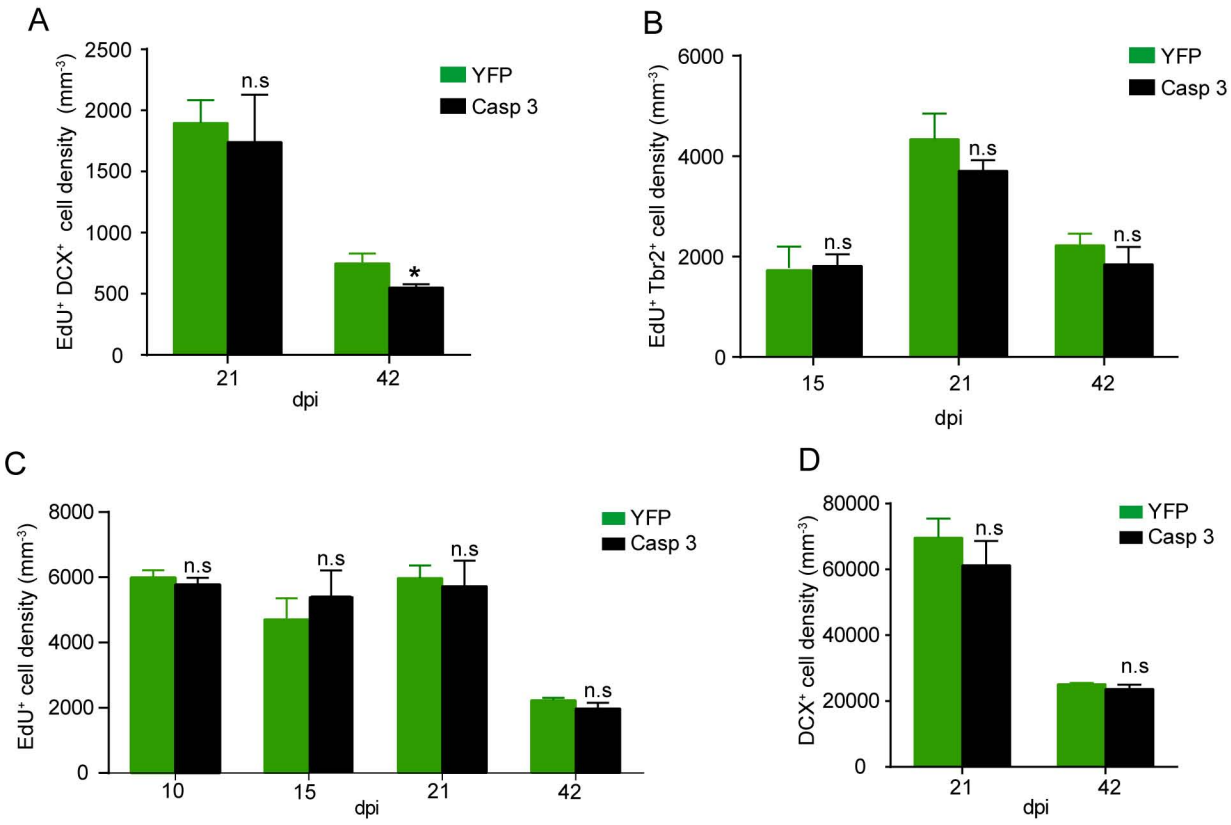

Figure S6. Yeh et al. 2018

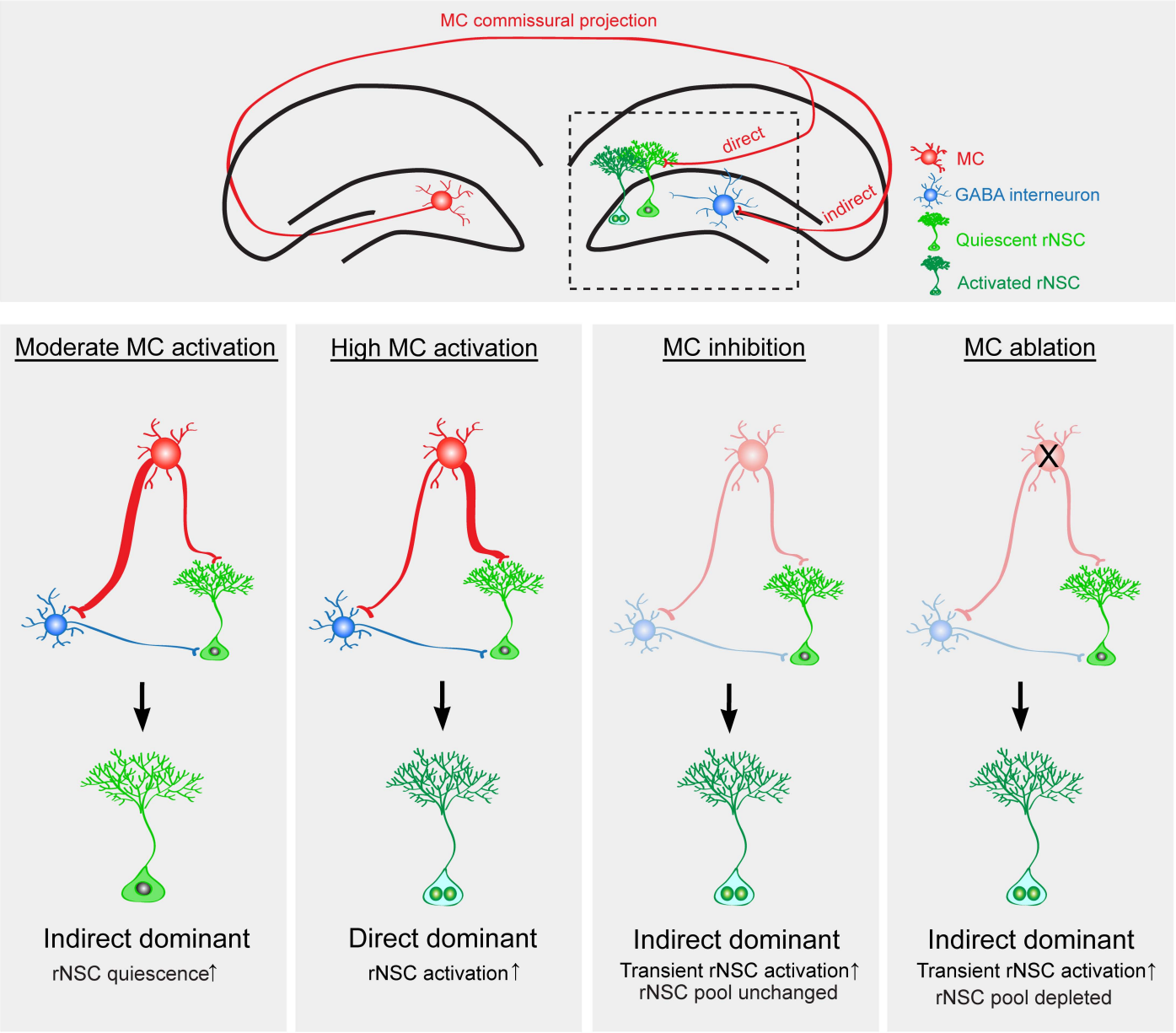

Figure S7. Yeh et al. 2018

Supplemental Figure Legends

Figure S1. Expression of NMDA NR1 subunits in rNSC fine processes in the inner molecular layer. Related to Figure 1.

(A) Coronal section of the mouse dorsal DG (GCL, granule cell layer; ML, molecular layer), showing an increased density of NR1-immunogold labelling in the first third of the ML.

(B) Dorsal DG labelled with NR1 immunogold and Nestin-GFP immunoperoxidase (DAB, 3,3-diaminobenzidine chromogen). Box, Nestin-GFP-DAB positive rNSC selected for quantification of NR1 immunogold particles in D,E.

(C) Higher magnification of A (SGZ, subgranular zone).

(D) Higher magnification of B.

(E) Low magnification (1,450×) electron microscopy (EM) image of region corresponding to cell in D; used for tracings, area measurements and immunogold quantification, arrows for comparison.

(F) High magnification (5,800×) images covering same region as D and E; used to instruct tracings, measurements and quantifications.

(G) Representative serial EM image (1 of 10 sampled sections, from 124 across the cell) showing the GCL primary process in blue, perisynaptic ML processes in green, mitochondria in pink, NR1-gold in yellow.

(H) Compressed image of the 10 serial sections sampled for analysis (rNSC process in white, NR1-gold in yellow).

(I-K) Two regions of the GCL primary process of a DAB-peroxidase-labelled rNSC, displaying NR1 gold particles; arrows point to membrane-associated particles and arrowheads to others.

(L-N) Perisynaptic ML rNSC processes displaying membrane-associated NR1 gold particles (arrows), directly apposing asymmetrical (putatively excitatory) synapses between axon terminals (a) and dendritic spines (s; m, mitochondria); M and N shown in two serial sections.

(O) Mean ratios of rNSC and control structure (+, positive; -, negative) gold densities (± standard error of the mean) relative to those of ML rNSC perisynaptic processes (control structure ratios compared to rNSC cell ratio) Scale bars: A, 100 µm; B, 20 µm; C- G, 10 µm; H, 5 µm; I-J, 1 µm; K-M, 0.5 µm.

Figure S2. Validation of dual viral labeling approach, characterization of rNSC morphological heterogeneity, and confirmation of direct pathway in rNSC depolarization using optogenetic approach. Related to Figure 2.

(A) Representative confocal image showing colocalization of mCherry signal and HA signal from animals injected with AAV-CaMKII-HA-hM3Dq-mCitrine and AAV-CaMKII-mCherry. Scale bar 100 µm.

(B) Sample confocal image of rNSCs from Nestin-GFP animals depicting the diversity in length of rNSC projections. Only a minority of rNSCs are long enough for the bushy heads reach the inner molecular band and interact with the commissural projections (labeled in red). Scale bar 50 µm.

(C) Proportion of Nestin-GFP$^+$ rNSCs with bushy heads reaching MC commissural projections at the inner molecular layer.

(D) Unilateral injection strategy of CaMKII-ChR2-mCherry in Nestin-GFP mice for acute-slice recording at the contralateral side and ChR2 terminal stimulation with 470 nm light.

(E) A sample fluorescence/DIC image and a representative whole-cell recording of a GFP$^+$ NSCs from the contralateral hemisphere with 470 nm LED light stimulation at 10 Hz in the presence of bicuculline.

(F-G) Sample trace showing GFP$^+$ rNSC responding to (F) single blue light flash or (G) a train of flashes in the presence of bicuculline and low concentration 4-AP.

Figure S3. CNO-dose dependent effects on MCs and contralateral GCL cells, and effects

of enriched environment (EE) on c-Fos expression in MCs and rNSC activation. Related to Figure 4.

(A) Sample Ca^{2+} signals showing dose-dependent increases in Ca^{2+} events induced by chemogenetic activation of GCaMP6f^{+} hM3Dq-mCherry^{+} MCs.

(B) Percentage of MCs that exhibited distinct Ca^{2+} events during each 10-minute epoch of increased CNO concentrations (0, 0.25 and 1 µM CNO).

(C) Quantification of mean calcium event frequency for 0, 0.25 and 1 µM CNO showing trending increase in detectable calcium events. (n=22 MCs, 2 mice).

(D) Distribution of c-Fos^{+} cells in the inner, middle, and outer GCL.

(E) Confocal images showing Nestin and EdU labelling in the DG; white arrow indicates active NSC (EdU^{+} Nestin^{+}) while orange arrow heads point to quiescent NSC (EdU^{-} Nestin^{+}). Scale bar 100, 50 µm. Higher magnifications on the right.

(F) Confocal images showing c-Fos expression in MCs (GluR2/3^{+} hilar cells) of mice housed in standard housing conditions (left) and EE (right). Arrows indicate c-Fos^{+} cells. Scale bar 10 µm.

(G-H) Increased percentage of GluR2/3^{+} c-Fos^{+} cells in the hilus after EE (G), despite unaltered number of GluR2/3^{+} cells (H) (n= 4 mice from each housing condition).

(I) Confocal images of c-Fos^{+} PV interneurons from mice under EE conditions. Boxed region is shown in higher magnification on the right. Scale bars 100, 20 µm.

(J) Percentage of PV^{+} c-Fos^{+} cells in the DG is unchanged in EE conditions (n=4 mice from each housing condition).

(K) Stereological quantification of Ki67^{+} rNSCs (n=4 mice from each housing condition).

Figure S4. Chemogenetic activation of MCs by CNO in acute brain slices. Related to Figure 5.

(A) Unilateral injection of DIO-hM3Dq-mCherry and DIO-GCaMP6s in the DG of 5htr2A-Cre mice.

(B) Fluorescent images in acute brain slices showing mCherry^{+} GCaMP6^{+} cells in the hilus. Scale

bar 20 μm.

(C) Sample fluorescent images of the cell indicated in the boxed region of B, and diverse Ca^{2+} responses in several MCs evoked by CNO.

Figure S5. Validation of chemogenetic inhibition of MCs by CNO in acute brain slices, and effects on rNSC activation and maintenance by cell-autonomous deletion of ionotropic glutamate receptors in rNSCs. Related to Figure 6.

(A) Unilateral injection of DIO-hM4Di-mCherry and DIO-GCaMP6s in the DG of 5htr2A-Cre mice.

(B) Sample images of a $GCaMP6^{+}$ $mCherry^{+}$ MC and CNO dependent Ca^{2+} transients.

(C) Sample fluorescence traces for the three cells indicated in B, depicting the quenching of spontaneous Ca^{2+} events by CNO-induced chemogenetic inhibition of MCs.

(D-H) Selective deletion of ionotropic glutamatergic receptors in rNSCs did not significantly alter rNSC behavior. (D) Breeding scheme and (E) TMX induction/EdU injection paradigm of *Gria1-3*$^{fl/fl}$; *Grin1*$^{fl/fl}$ (F4 control) and *Nestin-creER*$^{T2+/-}$; *Gria1-3*$^{fl/fl}$; *Grin1*$^{fl/fl}$ (cKO) mice. (F-H) Stereological quantification of EdU incorporation in density (F) and percentage (G), and the density of $GFAP^{+}$ rNSCs (H) in control and cKO mice (n=5).

Figure S6. Effects of chronic ablation of MCs on non-rNSC populations. Related to Figure 7.

(A-D) Stereological quantification of proliferation from several non-NSC populations at various time points after Cre-dependent caspase injections in 5htr2A-Cre animals. (A) density of proliferating $EdU^{+}DCX^{+}$ neuroblasts, (B) density of proliferating $EdU^{+}Tbr2^{+}$ intermediate progenitors, (C) density of EdU^{+} cells, and (D) density of DCX^{+} cells. (n=4,3,4,3 mice in control group; n=4,5,4,4 mice in caspase group).

Figure S7. Summary model of rNSC regulation by various MC activity states. Related to Figures 1-7. MC commissural projections provide direct glutamatergic and indirect GABAergic inputs to rNSCs. When MCs are activated at a moderate level, the indirect GABA pathway dominates and promotes rNSC quiescence. When MCs are activated at a high level, the direct glutamatergic pathway dominates and promotes rNSC activation. When MCs are inhibited, decreased GABAergic tone is profound, thus resulting in a transient NSC activation (without depleting the rNSC pool). MC ablation similarly results in profound reduction of the indirect pathway, but results in a transient increase of rNSC activation followed by rNSC pool depletion.